Acta Pharmaceutica Sinica B 2025;15(11):5891−5907

Chinese Pharmaceutical Association
Institute of Materia Medica, Chinese Academy of Medical Sciences

Acta Pharmaceutica Sinica B

www.elsevier.com/locate/apsb
www.sciencedirect.com

ORIGINAL ARTICLE

Ferrum@albumin assembled nanoclusters inhibit NF-κB signaling pathway for NIR enhanced acute lung injury immunotherapy

Xiaoxuan Guan[a,†], Binbin Zou[b,†], Weiqian Jin[c,†], Yan Liu[b], Yongfeng Lan[b], Jing Qian[d], Juan Luo[e], Yanjun Lei[e], Xuzhi Liang[c], Shiyu Zhang[c], Yuting Xiao[a], Yan Long[a], Chen Qian[a], Chaoyu Huang[a], Weili Tian[f], Jiahao Huang[b], Yongrong Lai[b,*], Ming Gao[c,*], Lin Liao[a,*]

[a]*Department of Clinical Laboratory, the First Affiliated Hospital of Guangxi Medical University, Key Laboratory of Clinical Laboratory Medicine of Guangxi Department of Education, Nanning 530021, China*
[b]*Department of Hematology, Department of Colorectal and Anal Surgery, the First Affiliated Hospital of Guangxi Medical University, Nanning 530021, China*
[c]*Department of Gynecology, the First Affiliated Hospital of Guangxi Medical University, Nanning 530021, China*
[d]*Cardiothoracic Surgery Intensive Care Unit, Cardiovascular Injury and Repair Engineering Research Center of Guangxi Department of Education, the First Affiliated Hospital of Guangxi Medical University, Nanning 530021, China*
[e]*Department of Endocrinology, Department of Intensive Care Unit, Hunan Provincial People's Hospital, the First Affiliated Hospital of Hunan Normal University, Changsha 410000, China*
[f]*Molecular Neurogenetics, German Cancer Research Center, Heidelberg 69120, Germany*

Received 30 June 2025; received in revised form 25 July 2025; accepted 2 August 2025

KEY WORDS

Acute lung injury;
Nanozyme;
Albumin nanocluster;
NIR enhanced therapy;
ROS scavenging;
Macrophage M2

Abstract Acute lung injury (ALI) has been a kind of acute and severe disease that is mainly characterized by systemic uncontrolled inflammatory response to the production of huge amounts of reactive oxygen species (ROS) in the lung tissue. Given the critical role of ROS in ALI, a Fe_3O_4 loaded bovine serum albumin (BSA) nanocluster (BF) was developed to act as a nanomedicine for the treatment of ALI. Combining with NIR irradiation, it exhibited excellent ROS scavenging capacity. Significantly, it also displayed the excellent antioxidant and anti-inflammatory functions for lipopolysaccharides (LPS) induced macrophages (RAW264.7), and Sprague Dawley rats *via* lowering intracellular ROS levels, reducing

*Corresponding authors.
E-mail addresses: laiyongrong@hotmail.com (Yongrong Lai), gaoming1983125@hotmail.com (Ming Gao), liaolin789@163.com (Lin Liao).
[†]These authors made equal contributions to this work.

Peer review under the responsibility of Chinese Pharmaceutical Association and Institute of Materia Medica, Chinese Academy of Medical Sciences.

https://doi.org/10.1016/j.apsb.2025.08.012

polarization;
NF-κB pathway inhibition;
Immunoregulation activation

inflammatory factors expression levels, inducing macrophage M2 polarization, inhibiting NF-κB signaling pathway, increasing $CD4^+/CD8^+$ T cell ratios, as well as upregulating HSP70 and CD31 expression levels to reprogram redox homeostasis, reduce systemic inflammation, activate immunoregulation, and accelerate lung tissue repair, finally achieving the synergistic enhancement of ALI immunotherapy. It finally provides an effective therapeutic strategy of BF + NIR for the management of inflammation related diseases.

1. Introduction

Acute lung injury (ALI) is a kind of acute hypoxic respiratory dysfunction induced by various factors. And it can damage alveolar epithelial cells and endothelial cells, causing diffuse interstitial and alveolar edema[1,2]. When it reaches a more severe level, acute respiratory distress syndrome (ARDS) with high mortality occurred[3]. ALI is mainly characterized by a systemic uncontrolled inflammatory response. In the metabolic process of lung tissue, excessive production of metabolites can deplete intracellular glutathione (GSH), causing the existence of excessive reactive oxygen species (ROS) in mitochondria. And mitochondrial dysfunction ultimately leads to the apoptosis of lung cells[4,5]. Meanwhile, excessive ROS participates in the generation of inflammatory factors including TNF-α, iNOS and IL-6, promoting oxidative stress response, and inducing cell death[6,7]. These effects lead to structural damage and functional impairment of lung tissue. Thus, the strategy focused on scavenging ROS and further reprogramming redox homeostasis is expected to be applied to prevent and treat the ROS-related diseases, including ALI. On the other hand, as a protein complex, nuclear factor kappa B (NF-κB) is a key nuclear transcription factor of cells. It is expressed in almost all animal cells and participates in cellular responses to stimuli such as free radicals, cytokines, and external stimuli. And it plays a central role in inflammatory response, immune response, and the regulation of cell apoptosis[8]. As a major regulator of inflammation, NF-κB can control many aspects of innate and adaptive immune responses, and its activation is connected to inflammation and autoimmune diseases[9,10]. Therefore, inhibiting NF-κB signaling pathways can be a target for inflammation treatment. In the Lancet, a study about ALI was published, revealing that it helped to improve lung damage by down-regulating the NF-κB signaling pathway, and upregulating the CAMP-Epac and HO-1 pathways[11]. Quan et al. developed a type of novel lappaconitine derivatives with a lot of substituent on 20-N position as potential anti-inflammatory agents. It demonstrated that these derivatives possessed an obvious anti-inflammatory mechanism *via* the inhibition of NF-κB and MAPK signaling pathways[12]. These studies suggested that inhibiting NF-κB would be beneficial for ALI clinical therapy. However, it is highly challenging how to inhibit NF-κB signaling in ALI, limited by the low biostability and biosafety of the inhibitors.

Benefiting from the advance of nanotechnology, nanomedicines have been widely applied in various diseases' therapy[13], including the strategies focusing on NF-κB signaling[14,15]. Nanosized Fe_3O_4, as a kind of nanozyme with multiple catalytic functions of superoxide dismutase (SOD), catalase (CAT) and glutathione peroxidase (GPX)[16], could be applied for various biomedical fields such as medical diagnosis[17,18], and disease therapy[19,20]. In addition, Fe element can participate in various physiological activities, and play a significant role in maintaining intracellular redox homeostasis[21]. Significantly, Fe_3O_4 nanoparticles (NPs) have been employed as ROS scavengers to alleviate inflammation-related diseases like acute kidney injury[22,23], Parkinson[24,25], skin repair[26,27], etc., attributed to the valence state transition between Fe ions[28] and oxygen vacancy to inhibit NF-κB signaling pathway[29,30]. Under near infrared (NIR) irradiation, it also confirmed the enhanced ROS scavenging capacities[31,32], and promoted tissue repair[33,34] of metal-based nanozymes, helpful to ALI therapy with high efficacy[35]. Meanwhile, drug delivery systems (DDSs) aim to systemically regulate the biodistribution of drugs in the human body in terms of time, space, and dosage[36]. For ALI therapy, it expects to deliver the appropriate amount of drugs to the correct location at the appropriate time, and also in a controllable release way, thus increasing their utilization efficiency, and minimizing toxic side effects[37,38]. Bovine serum albumin (BSA) is one of the most important molecules involved in transcytosis as a DDS due to the unique properties, including high drug loading, good water solubility, and nontoxicity[28,39]. Upon the binding of albumin to a set of albumin receptors, it was internalized and translocated to the targeted area, enabling specific drug delivery to the disease area[40]. On the other hand, albumin can provide a spatial confinement effect for NPs growth, and prevent their aggregation[41]. Thus, it had been widely used to fabricate DDSs for respiratory system disorders[42,43].

Herein, we reported a simple synthetic method of biocompatible Fe_3O_4 loaded BSA nanocluster (BF). It could scavenge multiple ROS, thereby efficiently reducing lipid peroxidation and inhibiting cell apoptosis. After being taken up by macrophages, it could efficiently clear intracellular ROS, downregulate inflammatory factors, induce macrophage M2 polarization, and inhibit the NF-κB signaling pathway (Fig. 1). Most significantly, combining with NIR irradiation, BF + NIR more efficiently reprogrammed lung redox homeostasis, activated immunoregulation, and accelerated lung tissue repair, to achieve synergistic enhanced immunotherapy of ALI. Altogether, the good biocompatibility, excellent ROS scavenging, and outstanding NF-κB pathway inhibition by the strategy of BF + NIR made it a promising candidate for the immunotherapy of inflammation related diseases.

2. Materials and methods

2.1. Chemical reagents

Iron chloride hexahydrate ($FeCl_3 \cdot 6H_2O$, 99%, Mw = 270.30), BSA (98%, Mw = 66.40), and sodium hydroxide (NaOH, 99%, Mw = 39.99) were supplied from Macklin (China). Lipopolysaccharides (LPS, ≥97%) and phosphate-buffered saline (PBS, pH = 7.4) were commercially supplied by Sigma-Aldrich (St. Louis, MO, US), and hydrogen peroxide (H_2O_2, 30% *w/w*, Mw = 34.01) was commercially obtained from Junobio (Nanning, China). Methanol (CH_4O, 99.5%, Mw = 32.04), anhydrous ethanol (C_2H_6O, ≥99.7%, Mw = 46.07). All chemicals were directly applied without further treatments.

2.2. Preparation of BF and its physicochemical characterization

The preparation of BF was implemented by a simple hydrothermal reaction in a weak alkaline condition[44,45]. Briefly, 1 g of BSA was homogeneously dissolved in deionized (DI) water, followed by the addition of 0.2 g $FeCl_3$. After stirring for 0.5 h, 0.2 g NaOH was added to the solution. The final mixture was reacted at 80 °C for 2 h. Finally, the final product was centrifuged to remove the supernatant and re-dispersed with DI water. The above procedures were repeated for 3 times, and BF was obtained after freezing-drying.

To characterize the zeta potential, morphology, crystallization structure, and molecular structure of BF, the zeta sizer (Malvern Instruments Ltd, Nano ZS90, Malvern, UK), transmission electron microscopy (Hitachi, HT7800, Tokyo, Japan), X-ray diffraction (Rigaku, MiniFlex 600, Tokyo, Japan), and Fourier transform infrared spectrometer (Shimadzu, IRTracer-100, Tokyo, Japan) were applied. And the thermal stability of BSA and BF was investigated by thermal gravity analyzer (TA, STD650, New Castle, DE, USA). Besides, the element composition and Fe element content of BF were investigated by X-ray photoelectron spectroscopy (Thermo Fisher Scientific, ESCALAB 250XI+, Waltham, MA, USA), as well as inductively coupled plasma-mass spectrometry (Varian, 820−MS, Palo Alto, CA, USA). To investigate the photothermal behaviors, BSA and BF with different concentrations (0, 50, 100 and 200 μg/mL) were irradiated by NIR imager of different laser intensities (808 nm, 1, 1.5 and 2 W/cm^2). The corresponding photothermal images and temperatures were recorded. Specifically, the photothermal stability was implemented by placing 200 μg/mL BF with NIR irradiation (2 W/cm^2, 15 min) for 4 "on" and "off" cycles. Significantly, BF or Fe_3O_4 was dispersed in different solutions (PBS, Dulbecco's modified Eagle medium (DMEM, Gibco, Billings, MT, USA), fetal bovine serum (FBS, Gibco, Billings, MT, USA), and 5 mmol/L H_2O_2) respectively. At 0, 0.5, 1, 2, 4, 8, 12 and 24 h, the solutions were photographed by the camera.

The ROS scavenging capacities were initially characterized by electron spin resonance (Bruker, A300, Karlsruhe, BW, Germany). Details were: BF with 100 μg/mL was mixed with the different working solutions: 5-*tert*-butoxycarbonyl 5-methyl-1-pyrroline-*N*-oxide (BMPO, 100 mmol/L), xanthione (10 mmol/L) and xanthione oxidase (XOD, 1 U/mL), and 2,2,6,6-tetramethylpiperidine (TEMPONE, 100 mmol/L) for ·OH, $\cdot O_2^-$ and $^1O_2$ testing respectively. After mixing for 10 min, the corresponding signal was recorded by ESR. In addition, the H_2O_2, ·OH and $\cdot O_2^-$ testing kits were applied to test the ROS clearing capacities of BF with different concentrations (100, 200 and 300 μg/mL) by following the corresponding protocols of the manufacturer. Specifically, for BF + NIR, NIR irradiation was implemented for 10 min with the power intensity of 2 W/cm^2 after mixing BF with different working solutions.

2.3. Biological functions investigation at the cellular level

Mouse monocyte macrophages (RAW 264.7), lung epithelial cells (BEAS-2B) and mouse epithelioid fibroblast cells (L929) were commercially purchased from American Type Culture Collection (ATCC, USA). And the cells were cultured in DMEM containing 10% FBS and 1% penicillin/streptomycin (Solarbio, China). During cell culture, the medium was replaced with fresh medium every 2 days, and the cultured cells were passaged when reaching above 85% confluence.

The cell viability was investigated by cell counting kit-8 (CCK-8, Biosharp, China). And the cells were seeded in a 96-well plate with the density of 1×10^5 per well before incubation with BSA, Fe_3O_4 or BF of concentrations ranging from 0, 5, 10, 20, 50, 100, 200 to 500 μg/mL for 24 h. After washing with PBS, the cells were incubated with 10 μL CCK-8 kit for another 1 h. The supernatant was finally observed at 450 nm by a microplate reader (Thermo Fisher, Multiskan FC). In addition, the cell protection ability was also investigated by live/dead staining (Beyotime Biotechnology, China). In brief, RAW264.7 cells at a density of 2×10^6 per well were cultured in a 6-well plate. After being induced by LPS (1 μg/mL) for 30 min, the cells were incubated with 100 μg/mL BSA or BF. Specifically, for BF + NIR, NIR irradiation (2 W/cm^2) was implemented 3 times within 24 h after incubating with BF, 10 min per time. And the treated cells were stained with calcein-AM/propidium iodide (Beyotime Biotechnology) for 10 min before washing with PBS 3 times. Finally, the cells were observed by a fluorescent microscope (Olympus, CKX53, Tokyo, Japan). Meanwhile, the effect of NIR irradiation on the viability of L929 was also investigated. After mixing with BF, NIR irradiation was implemented 3 times within 24 h, 0, 5, 10 or 15 min per time before evaluating the live cell ratio.

In addition, to investigate the cellular uptake ability, RAW264.7 cells were cultured in the confocal dishes at a density of 2×10^6, and incubated with Cy5-BF for 0, 3 and 6 h, respectively. And then the treated cells were washed 3 times with PBS before being fixed with 4% paraformaldehyde (PFA, Biosharp, China) for 10 min. Next, the cytoskeleton and nuclei of cells were respectively stained with actin-tracker green-488 (Actin, Biosharp, China), and 4′,6-diamidino-2-phenylindole dilactate (DAPI, Biosharp, China) following the manufacturer's protocols. At last, the cells were washed with PBS before being embedded in paraffin and imaged by confocal scanning microscopy (ZEISS, LSM 980, Oberkochen, BW, Germany). Specifically, to prepare Cy5-BF, 50 mg BF was dispersed in 50 mL ethanol, and mixed with 10 mg Cy5-PEG2000-NHS (Lumiprobe, China) overnight. After centrifuging at 12,000 rpm (Eppendorf, 5425 R, Hamburg, NI, Germany) for 30 min to remove the supernatant, and re-dispersion in ethanol 3 times, the final products (Cy5-BF) were collected by vacuum drying.

To investigate the antioxidant and anti-inflammatory abilities, an enzyme-linked immunosorbent assay (ELISA) was initially applied. In detail, the supernatant of treated cells was collected and tested by the corresponding ELISA kits (Meimian, China) by following their protocols. And the intracellular ROS levels were also analyzed by ROS testing probes, where 2′,7′-dichlorodihydrofluorescein diacetate (DCFH-DA,

Maokangbio, China) and dihydroethidium (DHE, Maokangbio, China) were applied to test the intracellular total ROS and $\cdot O_2^-$ levels of treated cells. The cultured medium of treated cells was replaced with fresh medium containing DCFH-DA or DHE. After incubating 30 min, the cells were washed with PBS for 3 times and fixed with 4% PFA. The cells were finally observed by a fluorescent microscope. Besides, the expression levels of inflammation related genes (TNF-α and SOD2), macrophage polarization genes (CD86 and CD206), and tissue repair genes (CD31 and HSP70) were analyzed using reverse transcription-quantitative polymerase chain reaction (RT-qPCR). Briefly, the total RNA was extracted by using an RNA extraction kit (Magen, China), and RT-qPCR was performed by using the LightCycler® System (Roche, Switzerland). And the relative gene expression was analyzed by the $2^{-\Delta\Delta Ct}$ method, and compared with the glyceraldehyde-3-phosphate dehydrogenase (GAPDH), applied as the reference.

Furthermore, the related protein expression levels were investigated by immunofluorescent staining. Briefly, the treated cells were initially fixed with PFA for 30 min before blocking with BSA. And the cells were separately incubated with primary antibodies: CD86, CD206, CD31 or HSP70 (1:1000 dilutions, Proteintech, China) at 4 °C overnight. After PBS washing 3 times, the cells were incubated with secondary antibody (Alexa Fluor 647-labeled Goat Anti-Rabbit IgG (H + L), 1: 10,000) (Beyotime Biotechnology) for another 1 h. Finally, after being stained with DAPI for 10 min, the cells were imaged by fluorescent microscopy.

At last, to confirm the anti-inflammation mechanism, Western blotting (WB) was applied to detect the pathway-related proteins' expression levels. In detail, the pre-treated cells were washed with ice-cold PBS, and treated with lysis buffer (Solarbio, China) containing protease and phosphatase inhibitors (Solarbio, China). After centrifuging for 15 min, the supernatant was collected, and its protein concentration was measured and adjusted a BCA protein assay kit (Beyotime, China). Subsequently, the proteins were separated by protein gel electrophoresis and transferred to a polyvinylidene fluoride (PVDF) membrane (IPVH00010, Millipore, USA). After being blocked with blocking buffer (Sharebio, China) for 20 min, the membrane was washed with tris buffered saline with Tween-20 (TBST, Sigma) 3 times. And then the membrane was incubated with primary antibodies (anti-p65, p-p65, IκBα and p-IκBα, Proteintech, China) for 2 h before being incubated with the secondary antibody (Goat Anti-Rabbit, Sangon, China) for another 2 h. Finally, the membrane was soaked in 1 mL of Ultra-Signal ECL Western blotting detection reagent (Beyotime, China) before scanning by an automatic chemiluminescence image analysis system (Bio-Rad, USA). In addition, their pathway-related genes (p65, p-p65, IκBα and p-IκBα) expression levels were also analyzed by RT-qPCR.

2.4. *In vivo animal experiments*

All experimental procedures were executed according to the protocols approved by the Animal Experiment Ethics Committee of Guangxi Medical University (No. 2025E0329). Sprague Dawley (SD) rats (180～220 g) were chosen, and treated following the local guidelines of the care and use of laboratory animals of Guangxi Medical University. All animals were euthanized through intravenous injection of excessive pentobarbital sodium (Sigma, P3761). To investigate the *in vivo* biodistribution, *in vivo* animal imaging systems (PerkinElmer, IVIS Lumina Series III, Waltham, MA, USA) were utilized after intratracheal (IT) injection of NPs. Briefly, the ALI rats were IT injected with 0.8 mL solutions (100 μg/mL Cy5 or Cy5-BF). At the predetermined time points (0, 0.5, 1, 2, 4, 8, 12 and 24 h), the corresponding organs including heart, liver, spleen, lung and kidney were collected, and imaged by IVIS with the excitation (646 nm) and emission wavelengths (664 nm). And the *in vivo* photothermal feasibility was evaluated by IT injection of 0.8 mL BF (100 μg/mL) into rats. After 2 h, the lung of rats was irradiated by NIR light (2 W/cm^2) for 10 min. The corresponding photothermal images and temperatures were collected and recorded at the predetermined time points.

In *in vivo* biosafety, the blood biocompatibility was first investigated by hemolysis testing. In brief, the blood was freshly collected from SD rats and centrifuged at 3000 rpm for 10 min to remove the serum. And 0.5 mL erythrocyte suspension was mixed with 0.5 mL BF solution with different concentrations: 0, 5, 10, 20, 50, 100, 200 and 500 μg/mL, where DI water was utilized as the control. After 1 h incubation, the mixture was centrifuged at 3000 rpm for 10 min before being observed by a microplate reader at 540 nm. The corresponding hemolysis ratio was calculated as Eq. (1):

$$\text{Hemolysis ratio}\,(\%) = \left[(OD_s - OD_n) \,/\, (OD_p - OD_n)\right] / 100 \qquad (1)$$

where OD_n, OD_p and OD_s were the optical density (OD) of negative control, positive control and samples, respectively. And the body weight of each rat was weighed every day within 7 days. And after 7 days, the blood from rats was analyzed using the fully automatic blood analyzer (Mindray, China). Additionally, the major organs were isolated. After fixation with 4% PFA, they were embedded and cut into sections. And the tissue slice was applied for hematoxylin and eosin (H&E) staining, followed by observation.

ALI animal models were established by cutting the neck to expose the trachea, followed by adding 1 mg/mL LPS (5 mg/kg) into the trachea[46]. SD rats were separately divided into 4 groups (n = 6): rats without treatments (sham group), and ALI rats with IT injection of 0.8 mL saline (ALI group), BF (100 μg/mL, BF), and BF (100 μg/mL) and NIR irradiation (BF + NIR). Specifically, NIR irradiation was implemented 3 times (2 W/cm^2, 10 min) at 1, 2 and 3 h after IT injection for BF + NIR. After establishing ALI models for 0.5 h, the corresponding treatments were implemented. And the blood and major organs were collected after 24 h. The blood indicators of blood samples were analyzed by the fully automatic blood analyzer. Besides, the blood was centrifuged to collect the serum, and its inflammation related factors expression levels were analyzed by ELISA following the corresponding protocols. Significantly, the fresh blood was collected to isolate the corresponding cells, and the number of $CD4^+$ and $CD8^+$ T cells in the blood was quantified by using flow cytometry after staining with the anti-$CD4^+$ and anti-$CD8^+$ primary antibodies (Biolegend, America).

Furthermore, the major organs were applied for further evaluation. And the lungs were photographed, and the corresponding wet/dry ratios were calculated by weighing the lung before and after drying. Similarly, the lung tissues were homogenized, and their inflammatory factors expression levels were analyzed by ELISA.

Finally, the isolated organs were fixed with 4% PFA overnight and cut into sections for the subsequent experiments. At the beginning, the organ sections were treated with H&E staining, and imaged by an Olympus microscope. And the corresponding images of lung tissues were evaluated by using the Smith scoring.

Specifically, after NIR irradiation, the skin of rats was imaged and observed at 0.1, 0.5, 1, 2, 4 and 8 h. At 8 h, the skin tissue was treated with H&E staining and graphed by an Olympus microscope. Besides, the ROS levels of lung tissue were tested by using the DHE probe. After nuclei staining by DAPI, the sections were imaged by a fluorescent microscope.

Meanwhile, for immunohistochemical and immunofluorescent staining, the slides of lung tissues were firstly incubated with the primary antibodies (rabbit polyclonal anti-TNF-α, IL-10, CD86, CD206, CD31, HSP70, $CD4^+$ or $CD8^+$, Servicebio, China). After PBS washing 3 times, the tissue slides were incubated with biotinylated or fluorescent-labeled secondary antibodies (Servicebio, China). After rinsing, the slides were graphed by using the Olympus microscope, and the average OD (AOD) or mean fluorescent intensity (MFI) was analyzed using ImageJ software. Meanwhile, the number of $CD4^+$ and $CD8^+$ T cells in lung tissues was also quantified using flow cytometry.

2.5. Statistical analysis

All results are expressed as mean ± standard deviation (SD), and the significance was defined as $^*P < 0.05$, $^{**}P < 0.01$, $^{***}P < 0.001$ and $^{****}P < 0.0001$, where * indicated the comparison with normal or sham group.

3. Results and discussion

3.1. Preparation and physicochemical characterization

BF was fabricated by the reduction reaction of $FeCl_3$ in BSA solution (Fig. 2A)[47,48]. In brief, 1 g BSA and 0.25 g $FeCl_3$ were dissolved in 100 mL DI water with magnetic stirring before the reduction of ascorbic acid solution (10 mL, 20 mg/mL). The mixture was reacted overnight before centrifuged at 10,000 rpm for 10 min, and then re-dispersion in DI water. After repeated for 3 times, BF was collected by freeze-drying. Compared to BSA (white) and Fe_3O_4 (umber), it became brown for BF after the *in situ* reduction of $FeCl_3$ (Supporting Information Fig. S1).

As shown in Fig. 2B, the corresponding zeta potential was -21.1 ± 1.3 mV for BSA, while no significant changes happened for Fe_3O_4 (-29.1 ± 0.5 mV) and BF (-21.9 ± 1.2 mV). Similarly, from FTIR results, no obvious changes were observed between BSA and BF (Supporting Information Fig. S2). From the above, it was confirmed that ultra-small Fe_3O_4 loading did not affect the zeta potential and molecular structure of BF, similar to those of BSA. In addition, the crystallization structure was also investigated. As displayed in Supporting Information Fig. S3, compared to BSA with two obvious peaks (9.4° and 20.6°), there was a broad peak observed from 12.4° to 49.4° for BF, and 3 significant peaks at 30.3°, 35.7° and 43.2°, possibly attributed to Fe_3O_4 loading. And from TEM-mapping images, the diameter of Fe_3O_4 nanocluster was 5.5 ± 1.5 nm in BF (Supporting Information Fig. S4). And the obvious C, N, O and Fe elements existed in BF (Fig. 2C). Furthermore, the weight remaining ratio was 24.41% for BSA, increased to 78.82% for BF and 95.52% for Fe_3O_4 respectively (Fig. 2D and Supporting Information Table S1). Similarly, from XPS results, compared to BSA with C, N and O elements existed, the extra Fe element happened for BF (Supporting Information Fig. S5). Compared to BSA, the weight loss ratio decreased, and the existence of Fe elements for BF was due to Fe_3O_4 loading. Significantly, after calculation, the Fe element content was $2.79 \pm 0.01\%$ for BF by ICP-MS (Supporting Information Table S2). The differences in Fe content obtained between TGA and ICP-MS were due to the residue of BSA itself during TGA testing.

From the above, it confirmed the successful fabrication of BF. Most importantly, after Fe_3O_4 loading, it did not obviously change the zeta potential, and molecular structure of BF compared to BSA[49-51]. However, Fe_3O_4 loading contributed to the existence of the Fe element, changed the crystallization structure, and decreased the weight loss ratio of BF.

3.2. Dispersion and stability, photothermal effect and ROS scavenging ability

For a clinic application, it is required that the nanomedicine be stable and well dispersed during blood circulation[52,53]. Thus, the dispersion of BF in different solutions was investigated. To simulate the cellular conditions, DMEM and FBS were applied. And 5 mmol/L H_2O_2 was considered to simulate the ROS condition of ALI[54]. As displayed in Supporting Information Fig. S6, Fe_3O_4 was homogeneously dispersed in all solutions in the beginning. And it fully deposited on the bottom of PBS at 0.5 h, and DMEM, FBS and H_2O_2 at 4 h. However, for BF, it was totally precipitated on the bottom of PBS, DMEM and FBS at 8 h, and H_2O_2 at 12 h. From here, it displayed the improved dispersion of Fe_3O_4 after forming BF.

Additionally, the photothermal effects of BF were also investigated. As imaged in Supporting Information Fig. S7, compared to PBS and BSA with no temperature change, the temperatures increased over time for BF with NIR irradiation (2 W/cm^2). As illustrated in i of Fig. 2E, the temperatures remained stable for PBS (28.2 °C) and BSA (27.9 °C), while it increased to 54.4 °C for BF in the same concentration (100 μg/mL) after 15 min irradiation (2 W/cm^2). And the temperatures sequentially increased to 28.2, 51.6, 54.4 and 62.0 °C for BF with the concentration of 0, 50, 100 and 200 μg/mL under 2 W/cm^2 NIR irradiation (ii of Fig. 2E). Similarly, for different irradiation intensity, the temperatures jumped from 38.0 to 52.9 °C for 100 μg/mL BF with irradiation intensity from 1 to 2 W/cm^2 (iii of Fig. 2E). Specifically, after 4 cycles of "on" and "off", it displayed the excellent photothermal stability (iv of Fig. 2E).

Finally, the ROS scavenging ability was tested by ESR and ROS testing kits. The intensity of magnetic fields corresponded to the ROS levels in ESR. As shown in i of Fig. 2F, for ·OH levels, compared to the control group with obviously strong intensity of magnetic fields, the corresponding intensity of BF decreased, and significantly declined in BF + NIR. It was the same tendency for $\cdot O_2^-$ and $^1O_2$ levels, with the intensity order of control group > BF > BF + NIR (ii and iii of Fig. 2F). Meanwhile, by ROS testing kits, the ·OH scavenging ratio was $25.0 \pm 1.2\%$ for BSA, increased to $41.0 \pm 0.4\%$ and $57.9 \pm 0.4\%$ for 100 μg/mL BF and BF + NIR (Supporting Information Table S3). And if increasing the concentration from 100 to 500 μg/mL, the ·OH scavenging ratio changed from $41.0 \pm 0.4\%$ to $55.8 \pm 0.8\%$ for BF (i of Fig. 2G and Supporting Information Table S4). Similarly, for $\cdot O_2^-$ and H_2O_2 scavenging capacities, it was $24.3 \pm 3.9\%$ and $17.0 \pm 1.0\%$ in BSA, $37.3 \pm 0.2\%$ and $42.8 \pm 0.2\%$ in BF, and $51.9 \pm 3.5\%$ and $70.4 \pm 0.3\%$ in BF + NIR. Increasing the concentration of BF to 500 μg/mL, the ROS scavenging ratios became $71.5 \pm 1.2\%$ and $69.6 \pm 0.5\%$ for $\cdot O_2^-$ and $^1O_2$ respectively (ii and iii of Fig. 2G). Previous studies had confirmed that BSA had a certain of

antioxidant capacity, which could capture harmful free radicals, and act as an antioxidant, thereby protecting cells from oxidative stress damage[55,56]. After hybridizing with nanozymes, the ROS scavenging capacities were enhanced[57,58]. Significantly, NIR irradiation was helpful in improving the electron transfer rate and the improved ROS scavenging ability[59,60]. And increasing the concentration of BF + NIR also contributed to high ROS scavenging ability.

3.3. Cell biocompatibility and cellular uptake ability

To investigate the biological functions at the cellular level, 3 types of cells were considered: RAW264.7, BEAS-2B and L929. As shown in Fig. 3A, BSA displayed excellent cell biocompatibility with the cell viability around 100% within the concentrations ranges from 0 to 500 μg/mL. However, for Fe_3O_4 alone, its cell viability was significantly declined with the increase in concentration. At 100 μg/mL, its cell viability was 32.9 ± 2.6% for RAW264.7 and 38.7 ± 1.0% for BEAS-2B. If increasing the concentration to 500 μg/mL, the corresponding cell viability decreased to 11.4 ± 2.9% and 6.9 ± 2.0% for RAW264.7 and BEAS-2B, respectively. Significantly, the cell viability was 83.5 ± 2.2% and 79.1 ± 0.3% for RAW264.7 and BEAS-2B, respectively, in BF, both above 79%. Thus, 100 μg/mL was considered as the dosage concentration applied for further experiments. And due to its high cytotoxicity, Fe_3O_4 alone was not considered for further experiments.

From the live/dead staining images of RAW264.7, compared to the normal group with little red fluorescence (dead cells), lots of red fluorescence was found for the control group. For BSA, it slightly decreased the red fluorescence. However, it was observed that BF efficiently decreased the red fluorescence, and increased the green fluorescence, enhanced by BF + NIR (Fig. 3B). After statistical analysis, the live cell ratio was 98.8 ± 0.2%, 66.5 ± 0.6%, 78.4 ± 1.3%, 89.7 ± 0.5% and 94.7 ± 0.8% in normal group, control group, BSA, BF and BF + NIR respectively (Fig. 3C). It had confirmed that BF could efficiently protect the cells away from the damages of oxidative stress, and increased the live cell ratio. And this function had significantly been improved by BF + NIR due to its enhanced ROS scavenging capacities. It confirmed the good biocompatibility and protection ability of BF. Specifically, for L929, after NIR irradiation at different time points, only a few dead cells were observed (Supporting Information Fig. S8A). And the live cell ratio was 96.1 ± 0.8%, 95.6 ± 1.2%, 94.9 ± 0.8% and 95.9 ± 0.7% in BF + NIR with 0, 5, 10 and 15 min irradiation (Supporting Information Fig. S8B). From the above, BF effectively increased the cell viability of Fe_3O_4-based nanozymes, and BF + NIR had no damage to normal cells.

For clinical application, it is expected that nanomedicines could be easily taken up by cells, and exert their functions at the intracellular levels. As displayed in Supporting Information Fig. S9, the red fluorescence increased over time, indicating the increased uptake of BF. After analysis, the MFI was 4.8 ± 0.8 for BF at 3 h, increased to 11.1 ± 0.8 at 6 h (Supporting Information Fig. S10). From the TEM images, the quantified diameter of the nanocluster was less than 10 nm, which is helpful in improving the cellular uptake[61]. And the endocytosis of macrophages also contributed to the improved uptake of BF[62]. Thus, the good cellular uptake ability of BF was helpful in exerting its intracellular biological effects.

3.4. Antioxidant and anti-inflammatory capacities

LPS is a main component of the outer wall of Gram-negative bacteria. It can activate inflammatory cytokines expression and trigger an inflammatory response by binding with receptors on the surface of host cells, such as TLR4[63,64]. Thus, it is commonly used in cell experiments to simulate inflammatory responses. In animal models, it is mainly used to establish various inflammation-related disease models, such as ALI[65,66]. The *in vitro* antioxidant and anti-inflammatory capacities were initially evaluated by testing the expression of inflammatory factors in the supernatant of treated cells by ELISA. As shown in Fig. 3D, compared to the normal group with the low levels of IL-6 (8.7 ± 0.2 pg/mL) and TNF-α (43.1 ± 1.0 pg/mL) expression, they were significantly increased to 26.4 ± 0.8 and 98.9 ± 3.5 pg/mL for the control group. BSA slightly decreased the IL-6 (17.8 ± 0.2 pg/mL) and TNF-α (67.4 ± 0.6 pg/mL) expression levels, significantly enhanced by BF (13.1 ± 0.4 and 52.7 ± 0.6 pg/mL) and BF + NIR (10.4 ± 0.8 and 44.4 ± 2.0 pg/mL).

Next, from Fig. 3E, the intracellular ROS levels (DCFH-DA and DHE) of treated cells are displayed. In the normal group, they were in the lowest levels with almost no fluorescence observed. After LPS stimulation, they were significantly increased with a lot of fluorescence existed, where green and red fluorescence corresponded to the DCFH-DA and DHE levels of treated cells, respectively. Treatment by NPs could decrease their levels, especially for BF + NIR. After quantified analysis, the MFI of DCFH-DA was 19.5 ± 0.6, 41.4 ± 2.9, 30.9 ± 3.2, 29.0 ± 1.5 and 25.4 ± 2.4 respectively in the normal group, the control group, BSA, BF and BF + NIR. And the highest MFI of DHE was 44.4 ± 2.7 for the control group, followed by BSA (39.1 ± 3.6), BF (34.6 ± 3.3), BF + NIR (23.4 ± 2.5) and the normal group (16.0 ± 0.2) (Fig. 3F).

In addition, the related gene expression levels were analyzed by RT-qPCR, and illustrated in Fig. 3G. The TNF-α expression was in the lowest levels in the normal group (1.0 ± 0.3), significantly increased to 5.2 ± 0.4 for control group. Treatments by BSA, BF and BF + NIR could decrease its expression levels to 4.5 ± 0.1, 4.0 ± 0.2 and 1.3 ± 0.1, respectively (i of Fig. 3G). In contrast, for SOD2 expression levels, it was 1.0 ± 0.1 for the normal group, reduced for the control group (0.2 ± 0.1). Treatments improved the SOD2 expression levels. Among them, BF + NIR (0.8 ± 0.1) was the most, followed by BF (0.7 ± 0.1) and BSA (0.5 ± 0.1) (ii of Fig. 3G). Significantly, for CD31 expression, it was in the relative low levels in the normal group (1.0 ± 0.1), the control group (1.2 ± 0.1), BSA (1.9 ± 0.1) and BF (1.7 ± 0.1), significantly enhanced for BF + NIR (5.4 ± 0.2) (iii of Fig. 3G). It was in a similar tendency for HSP70 expression levels, where it was 10.4 ± 0.2 for BF + NIR, higher than that of the normal group (1.0 ± 0.1), the control group (1.6 ± 0.1), BSA (1.5 ± 0.1) and BF (1.0 ± 0.1) (iv of Fig. 3G).

Furthermore, immunofluorescent staining was also applied to test the corresponding CD31 and HSP70 expression levels. As displayed in Fig. 3H, the green fluorescence, corresponding to the CD31expression levels, was at relatively low levels in the normal group, the control group and BSA, slightly increased for BF, and significantly increased for BF + NIR. By statistical analysis, the MFI was 7.2 ± 2.0, 7.1 ± 1.2, 11.3 ± 0.9, 18.9 ± 1.1 and 44.1 ± 4.5 in the normal group, the control group, BSA, BF and BF + NIR respectively (Fig. 3I). Similarly, the expression of HSP70 was in relative low levels for all groups except for BF + NIR with obvious green fluorescence observed (Fig. 3J).

And the MFI was 6.3 ± 0.8, 6 ± 0.9, 6.1 ± 0.5 and 11.9 ± 1.6 for the normal group, the control group, BSA and BF, increased to 19.6 ± 1.8 for BF + NIR (Fig. 3K).

From the above, it confirmed the unique antioxidant and anti-inflammatory capacities of BF, enhanced by BF + NIR. For BSA itself, with a few amino acid residues, it possessed a little of antioxidant and anti-inflammatory capacities[67]. And for Fe_3O_4-based nanozymes with multiple catalytic functions, the original cytotoxicity limited their clinical application. After forming BF, it not only improved the biocompatibility of Fe_3O_4-based nanozymes, but also improved the dispersion of NPs to promote their catalytic functions[68]. Significantly, NIR irradiation was helpful in accelerating the movement of metal charges, contributing to high catalytic functions[69-71]. Thus, the strategy of BF + NIR most efficiently lowered the intracellular ROS levels, decreased the expression of inflammatory factors, promoted the expression of factors and accelerated the expression of tissue repair factors, presenting the most outstanding antioxidant and anti-inflammatory activities.

3.5. *In vivo biosafety study*

For clinic application, it is required that NPs could be accumulated in the lung, retained for a certain time, and gradually cleared from the lung[72,73]. As displayed in Fig. 4A, the fluorescence was only observed in the lung, while no fluorescence was observed in other organs. It indicated that NPs were only accumulated in the lung by IT administration, and could not be retained in other organs. And for Cy5 itself, the fluorescence appeared slightly at 0.5 h, increased to the highest levels at 2 h, and gradually disappeared after 8 h. However, for Cy5-BF, it reached the highest levels at 2 h, and was cleared after 12 h, confirming that BF could be accumulated in the lung for 12 h by IT injection (Fig. 4B). In the meantime, *in vivo* photothermal behaviors were also evaluated. As shown in Fig. 4C, the temperatures did not change over time for the sham group. Conversely, the temperature increased during NIR irradiation for BF. After statistical analysis, it maintained at 37.3 °C for sham group, while it shifted to 48.2 °C for BF after 15 min NIR irradiation (Fig. 4D). NIR light with the wavelength ranging from 700 to 1100 nm can be applied as an ideal light source for photodynamic therapy (PDT) and photothermal therapy (PTT), as it has excellent capability of penetrating the tissue, and little damages to healthy tissues[74,75]. Thus, NIR irradiation (808 nm) could be applied for PPT of ALI.

In *in vivo* therapy, the blood biocompatibility of BF was also considered. As displayed in Supporting Information Fig. S11, compared to the positive control with obvious hemolysis, there was no hemolysis observed for BF with the concentration ranges from 0 to 500 μg/mL. The corresponding hemolysis ratio was around 0.3%, all below the normal value (5%)[76,77]. Besides, after IT injection of BF + NIR, the body weight in rats gradually increased *versus* time, closed to that of sham group (Fig. 4E). And from the results of blood indicators, there were also no obvious differences observed between sham group and BF + NIR after 14 days (Fig. 4F and Supporting Information Table S5). Significantly, from H&E staining images, there were also no obvious differences existed in all major organs of sham group and BF + NIR (Fig. 4G).

To sum up, it demonstrated the feasibility of the strategy of BF + NIR for *in vivo* ALI therapy. And it also provided the proof that BF is only retained in the lung rather than other organs, and is gradually cleared. For long-term biosafety, it also confirmed that the strategy of BF + NIR did not affect the body weight, blood routine, liver and kidney function, and coagulation indicators, and pathological features of major organs, close to those of the sham group after 14 days.

3.6. *In vivo therapy evaluation*

The ALI models were established by IT instillation of LPS, and *in vivo* therapy was also implemented by IT administration[78,79]. The reason for the IT instillation of LPS applied to establish ALI models is due to the fact that no extra damages happen to other organs except for the lung during modeling[80]. And IT administration is a treatment method that directly delivers drugs through the respiratory tract, allowing the drugs to quickly act on the lungs or the whole body. Its core advantages lie in high local concentration, fast onset, and minimal systemic side effects. However, although nebulization administration is relatively convenient, it is not suitable for the operations in animal experiments[81,82]. The corresponding time schedule of the *in vivo* experiment is shown in Fig. 5A. As a results of IVIS, the strongest fluorescence was observed at 2 h by IT administration. Thus, NIR irradiation was implemented at 1, 2 and 3 h after IT administration during ALI therapy. After 24 h therapy, the blood and major organs were collected for investigation. As illustrated in Supporting Information Fig. S12 and Table S6, the blood indicators, including RBC, PT and TT, did not obviously change in all groups. And compared to the sham group, the PLT and MCV in the ALI group decreased, improved for BF and BF + NIR. Conversely, the WBC was at high levels for the ALI group, decreased in the order of BF > BF + NIR > sham group. Significantly, from the ELISA results of blood serum, the IL-6 and TNF-α expression were in the lowest levels for the sham group (12.3 ± 0.2 and 3.0 ± 0.2 pg/mL), significantly enhanced for the ALI group (23.6 ± 0.7 and 88.6 ± 1.9 pg/mL). BF (20.9 ± 0.3 and 62.7 ± 0.7 pg/mL) and BF + NIR (13.6 ± 0.7 and 23.2 ± 1.3 pg/mL) both decreased their expression, where BF + NIR played the most key role (Fig. 5B).

Next, the ALI therapy evaluation mainly focused on the lungs[83]. From the gross view of lungs, it was smooth, and in a pink color without congestion observed in the sham group. However, an obvious congestion phenomenon happened in the lungs of the ALI group, alleviated in the BF and BF + NIR. Especially for BF + NIR, the lung became smooth, and almost no congestion was presented (Fig. 5C). Meanwhile, the wet/dry ratio of lung tissue was 4.2 ± 0.1 in sham group, increased to 4.6 ± 0.1, 4.5 ± 0.1 and 4.2 ± 0.1 for ALI group, BF and BF + NIR respectively (Fig. 5D). And the expression levels of inflammation related factors in lung tissue were initially investigated by ELISA. As shown in Fig. 5E, the IL-6 and TNF-α expression was in the lowest levels in sham group (12.9 ± 0.5 and 3.6 ± 0.3 pg/mL), significantly ascended to 28.2 ± 0.3 and 79.5 ± 2.4 pg/mL in ALI group, and sequentially changed to 19.1 ± 1.1 and 53.9 ± 0.2 pg/mL for BF, and 13.6 ± 0.1 and 18.7 ± 0.6 pg/mL for BF + NIR.

Furthermore, the ROS levels in lung tissue were evaluated by the DCFH-DA testing probe. As shown in Fig. 5F, the ROS levels (green fluorescence) were the highest in the lung tissue of the ALI group, followed by the BF, BF + NIR and the sham group. After statistical analysis, the MFI was 10.4 ± 1.6, 44.9 ± 2.8, 32.0 ± 4.2 and 14.7 ± 1.6 in the sham group, ALI group, BF and BF + NIR, respectively (Supporting Information Fig. S13). And the H&E images of lung tissue were displayed in Fig. 5G. Compared to the sham group with a thin lung wall and no infiltration of inflammatory cells, obviously thickened lung wall and

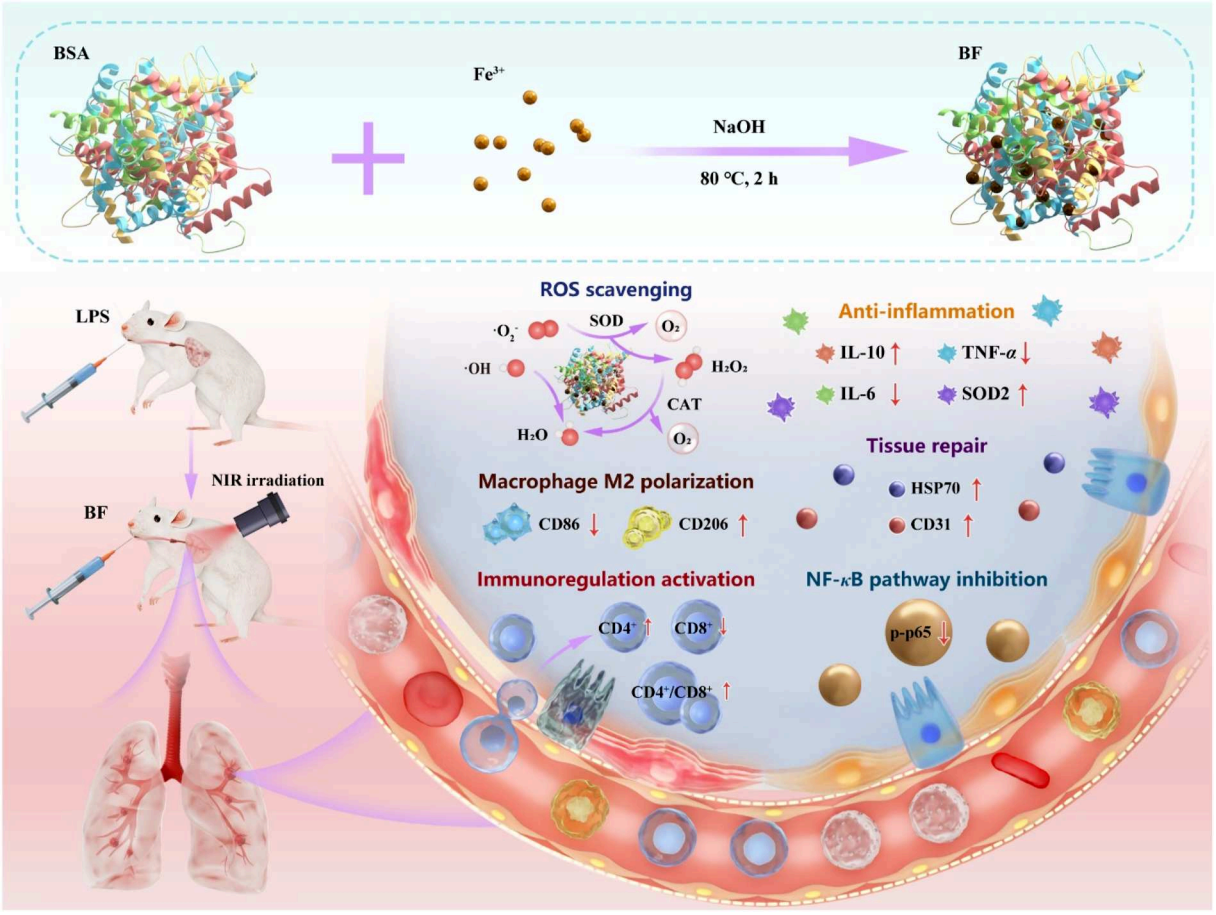

Figure 1 Schematic illustration of the preparation of BF, and the strategy of BF + NIR for ALI immunotherapy *via* the synergistic effects of intracellular ROS scavenging, inflammatory factors expression downregulation, macrophage M2 directional polarization, NF-κB pathway inhibition, $CD4^+/CD8^+$ ratio increase, and tissue repair factors upregulation to reprogram lung redox homeostasis, activate immunoregulation and accelerate lung tissue repair.

many inflammatory cells were observed in the ALI group. BF and BF + NIR efficiently decreased the thickness of the lung wall and the number of inflammatory cells, where BF + NIR was the most efficient. After Smith scoring, it was 3.7 ± 0.1 for the ALI group, sequentially decreased to 2.3 ± 0.1 for the BF, 1.4 ± 0.1 for the BF + NIR, and 0.8 ± 0.1 for the sham group (Fig. 5H). Besides, the TNF-α and IL-10 expression levels of lung tissue were investigated by immunohistochemical staining. As revealed in Fig. 5I, the TNF-α expression of lung tissue was in low levels in the sham group, significantly increased for the ALI group. It was also at higher levels for BF, decreased for BF + NIR. After quantified analysis, the AOD was 0.6 ± 0.1 for sham group, increased to 1.1 ± 0.1 for ALI group, and became 0.9 ± 0.1 for BF, and 0.7 ± 0.1 for BF + NIR, respectively (Fig. 5J). Conversely, the IL-10 expression levels of lung tissue were in the order of BF + NIR (1.6 ± 0.1) > BF (1.4 ± 0.1) > ALI (1.2 ± 0.1) > sham group (0.9 ± 0.1) (Fig. 5K and L). Significantly, the CD31 and HSP70 expression in lung tissue were also assessed. For CD31 expression, it was in the relatively low levels for the lung tissue of the sham group, ALI group, and BF, obviously enhanced for BF + NIR (Supporting Information Fig. S14). By quantified analysis, the AOD was all 0.5 ± 0.1 in the sham group, ALI group, and BF, increased to 0.9 ± 0.1 for BF + NIR (Supporting Information Fig. S15). And the HSP70 expression levels were the highest for the lung tissue of BF + NIR (1.1 ± 0.1), followed by ALI group (0.5 ± 0.1), BF (0.5 ± 0.1), and sham group (0.4 ± 0.1) (Supporting Information Figs. S16 and S17).

Finally, the skin tissue of treated rats was also observed. As shown in Supporting Information Fig. S18, no obvious skin damage occurred in rats after BF + NIR treatment. From H&E staining images, no significant differences existed between the skin tissue of the sham group and BF + NIR (Supporting Information Fig. S19). And the pathological features of other organs were also assessed by H&E staining. As shown in Supporting Information Fig. S20, no significant differences were observed for other tissue among all groups, indicating no damage to other organs during establishing the modeling and *in vivo* ALI therapy.

During ALI model establishment, the IT instillation of LPS was expected to ensure the successful establishment of lung models, with no or few effects on other organs. And IT administration was applied for ALI therapy to achieve high efficacy and minimum side effects. Thus, it had confirmed that the strategy of BF + NIR by IT injection could most efficiently decrease ROS levels, lower inflammatory factors expression levels, and accelerate the expression levels of repair factors in lung tissue. And this strategy also did not cause any extra damage to other organs, including skin, during therapy.

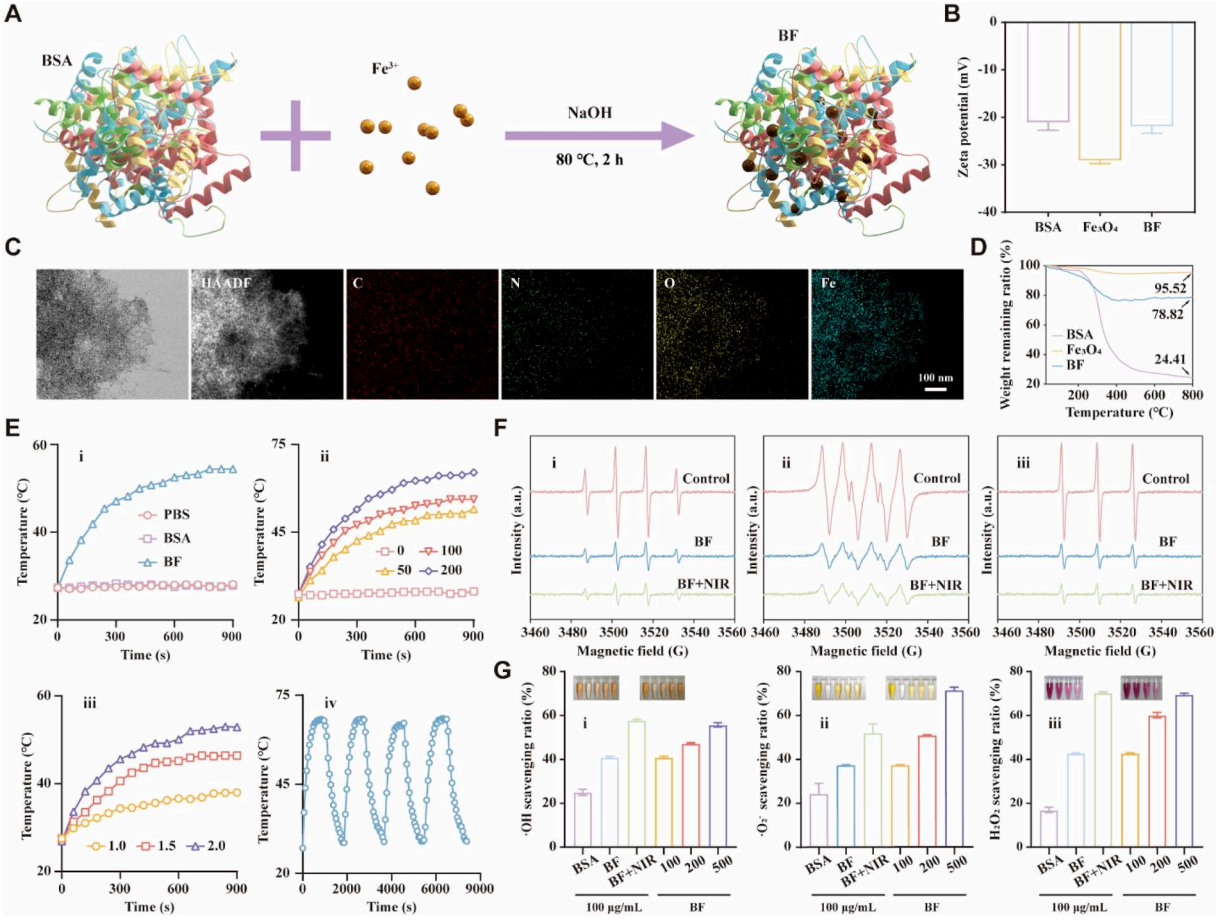

Figure 2 Preparation and physicochemical characterization of BF. (A) Schematic preparation of BF. (B) Zeta potential of BSA, Fe_3O_4 and BF. (C) TEM-mapping images of BF, and the corresponding element composition (HAADF, C, N, O and Fe images). Scale bar = 100 nm. (D) TGA results of BSA, Fe_3O_4 and BF. (E) Temperature changes of PBS, BSA and BF with the same concentration of 100 μg/mL under NIR irradiation (2 W/cm^2) (i), different concentration (0, 50, 100 and 200 μg/mL) of BF under NIR irradiation (2 W/cm^2) (ii), and 100 μg/mL BF under different power intensity of NIR irradiation (1, 1.5 and 2 W/cm^2) (iii) *versus* time, and photothermal stability of 200 μg/mL BF under NIR irradiation (2 W/cm^2) for 4 "on" and "off" cycles (iv). (F) ROS scavenging ability of BF and BF + NIR by ESR: ·OH (i), $\cdot O_2^-$ (ii) and $^1O_2$ (iii). (G) ROS scavenging capacity by CAT (i), ·OH (ii) and H_2O_2 (iii) testing kits: different NPs with 100 μg/mL, and BF with different concentrations.

3.7. ALI immunotherapy investigation

Immunotherapy is generally a treatment method that improves the body's immune function, and alleviates diseases, suitable for regulating various inflammatory responses[84-86]. It can also reduce tissue damage and organ dysfunction by regulating the immune function of the human immune system[87]. At the cellular level, the CD86 expression, corresponding to green fluorescence, was at the lowest levels for the normal group, and was obviously enhanced for the control group. And BSA could slightly decrease the green fluorescence of the control group, while BF and BF + NIR most efficiently decrease CD86 expression levels. By quantified analysis, the MFI was 1.9 ± 0.4 in normal group, changed to 34.0 ± 4.8, 12.3 ± 0.5, 5.9 ± 0.8 and 2.0 ± 0.5 for the control group, BSA, BF and BF + NIR, respectively (Fig. 6A and B). Conversely, CD206 expression was in the relative low levels in the normal group, control group, BSA and BF with little green fluorescence observed, significantly enhanced for BF + NIR (Fig. 6C). And the MFI of CD206 expression was in the order of BF + NIR (12.3 ± 0.8) > BF (9.3 ± 0.5) > BSA (7.1 ± 0.5) > control group (4.4 ± 0.3) > normal group (2.9 ± 0.8) (Fig. 6D). In addition, the expression levels of CD86 and CD206 genes were also analyzed by RT-qPCR. As illustrated in i of Fig. 6E, CD86 gene expression levels were 1.0 ± 0.3 for the normal group, jumped to 80.0 ± 8.1 for the control group. And they were sequentially declined to 68.9 ± 7.6 for BSA, 59.6 ± 0.9 for BF and 1.9 ± 0.3 for BF + NIR. And the expression levels of CD206 were 1.0 ± 0.1 for the normal group, sequentially ascended to 1.8 ± 0.1 for the control group, 3.0 ± 0.1 for BSA, 3.1 ± 0.1 for BF and 4.2 ± 0.1 for BF + NIR (ii of Fig. 6E). Furthermore, the macrophage polarization levels in lung tissue were also investigated. As shown in Fig. 6F, CD86 was at a high expression level in the ALI group, while it decreased for other groups. However, CD206 was in the lowest expression levels for the sham group, and it became the highest expression levels for BF + NIR. After quantified analysis, the AOD of CD86 expression was 0.6 ± 0.1 in the lung tissue of the sham group, significantly increased to 1.4 ± 0.1 for the ALI group. And the corresponding AOD was declined to 1.2 ± 0.1 and 0.9 ± 0.1 for BF and BF + NIR respectively (i of Fig. 6G). However, the AOD

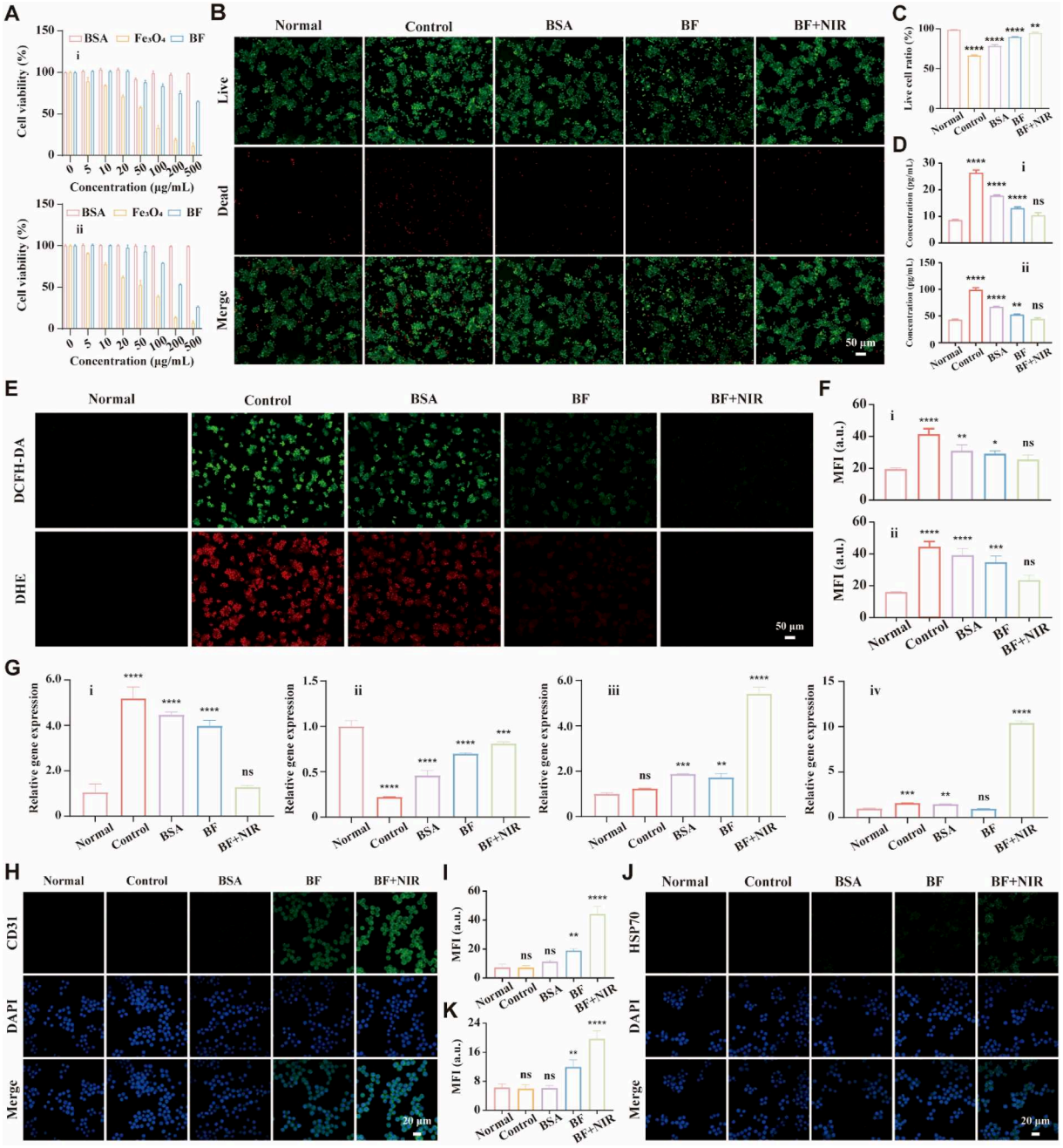

Figure 3 (A) Cell viability of BSA, Fe_3O_4 and BF with different concentrations ranging from 0 to 500 μg/mL: RAW264.7 (i) and BEAS-2B (ii). (B) Live/dead staining images of treated cells, and the corresponding live cell ratio (C). Scale bar = 50 μm. Data are presented as mean ± SD (n = 3). (D) Inflammatory factors (IL-6 (i) and TNF-α (ii)) expression levels of the supernatant of treated cells by ELISA. (E) Intracellular ROS levels of treated cells by fluorescent microscopy, and the corresponding MFI (F): DCFH-DA (i) and DHE (ii). Scale bar = 50 μm. Data are presented as mean ± SD (n = 3). (G) Relative gene expression levels of treated cells by RT-qPCR: TNF-α (i), SOD2 (ii), CD31 (iii) and HSP70 (v). (H) CD31 expression levels of treated cells by fluorescent microscope, and the corresponding MFI (I). Scale bar = 20 μm. Data are presented as mean ± SD (n = 3). (J) HSP70 expression levels of treated cells by fluorescent microscope, and the corresponding MFI (K). Scale bar = 20 μm. Data are presented as mean ± SD (n = 3). The corresponding groups were: cells without treatment (normal group), cells pre-treated with LPS followed by incubating with PBS (control group), 100 μg/mL BSA (BSA), 100 μg/mL BF (BF), and 100 μg/mL BF and NIR irradiation (2 W/cm^2) (BF + NIR). Data are expressed as mean ± SD. One-way ANOVA analysis was conducted to test for differences among groups. "*" symbol compared with normal group, *$P < 0.05$, **$P < 0.01$, ***$P < 0.001$, and ****$P < 0.0001$; and ns, not significant.

of CD206 expression was the highest for BF + NIR (1.2 ± 0.1), sequentially reduced for BF (0.9 ± 0.1), ALI group (0.7 ± 0.1) and sham group (0.5 ± 0.1) (ii of Fig. 6G). The downregulation of CD86 and upregulation of CD206 expression levels indicated the macrophage M2 directional polarization by the strategy of BF + NIR.

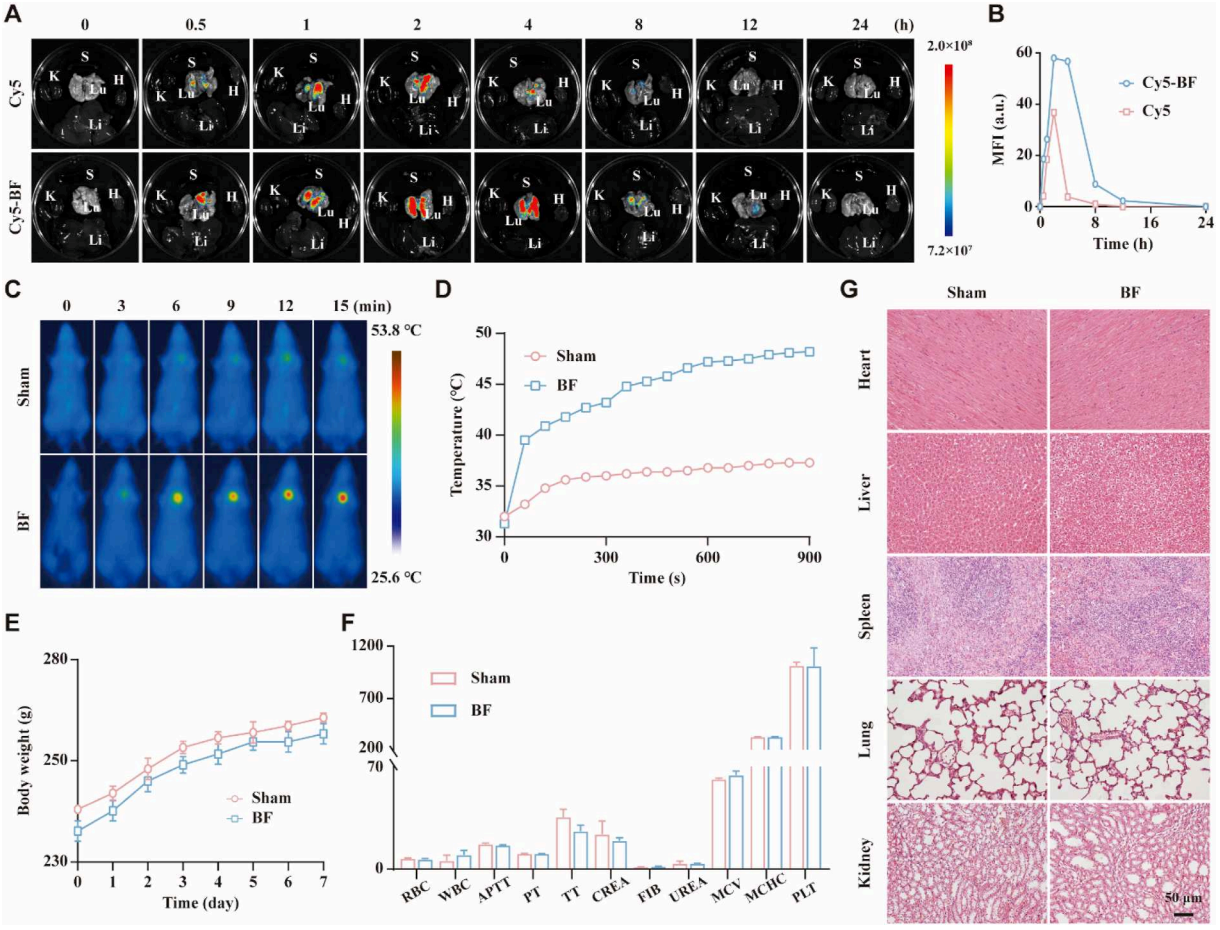

Figure 4 (A) *In vivo* bio-distribution of Cy5 and Cy5-BF after IT injection. The fluorescent images of major isolated organs (heart (H), liver (Li), spleen (S), lung (Lu) and kidney (K)) of treated rats at predetermined time points (0, 0.5, 1, 2, 6 and 24 h) by IVIS, and the corresponding MFI of lung (B). The corresponding groups were: rats injected with Cy5 (Cy5), and Cy5-BF (Cy5-BF). (C) *In vivo* photothermal feasibility of BF, and the corresponding temperature changes *versus* time (D). (E) Body weight changes of treated rats *versus* time. (F) Blood indicators of treated rats. (G) H&E staining images of the major organs of treated rats. Scale bar = 50 μm. Data are presented as mean ± SD (n = 6). The corresponding groups were: rats without treatment (sham group) and rats with BF injection (BF).

In addition, the $CD4^+$ and $CD8^+$ T cells number was also analyzed by immunofluorescent staining and flow cytometry. As shown in Supporting Information Fig. S21, for blood samples, the $CD4^+$ T cells number was 47.2 ± 0.1%, 46.5 ± 0.2%, 55.3 ± 0.5% and 59.9 ± 1.1% in the sham group, the ALI group, BF and BF + NIR respectively, while it was 48.0 ± 0.1%, 48.7 ± 0.4%, 37.8 ± 0.4% and 32.9 ± 0.7% for $CD8^+$ T cells number in the sham group, the ALI group, BF and BF + NIR respectively. After calculation, the $CD4^+/CD8^+$ ratio was 1.0 ± 0.1 for the sham group, and 1.0 ± 0.1 for the ALI group, sequentially increased to 1.5 ± 0.1 for BF, and 1.8 ± 0.1 for BF + NIR (Supporting Information Fig. S22). Besides, the $CD4^+$ and $CD8^+$ T cells number in lung tissue was also quantified and analyzed by flow cytometry. As displayed in Fig. 6H, the number of $CD4^+$ and $CD8^+$ T cells was in a small amount in the lung tissue of the sham group (25.6 ± 0.4% and 26.9 ± 0.3%) and the ALI group (24.3 ± 0.6% and 26.2 ± 0.7%). For the lung tissue of BF, the $CD4^+$ T cells number increased to 31.3 ± 0.4%, and the $CD8^+$ T cells number remained at the same levels (26.5 ± 0.6%). Significantly, the $CD4^+$ T cells was increased to 31.6 ± 1.5%, and the number of $CD8^+$ T cells decreased to 24.6 ± 0.2%. After calculation, the $CD4^+/CD8^+$ ratio was 1.0 ± 0.1 and 0.9 ± 0.1 for the sham group and the control group, increased to 1.2 ± 0.1 and 1.3 ± 0.1 for BF and BF + NIR (Fig. 6I). Finally, the number of T cells in lung tissue was also analyzed. For immunofluorescent staining of lung tissue, the green fluorescence corresponded to the number of $CD4^+$ T cells, while red fluorescence was equal to the number of $CD8^+$ T cells. As displayed in Fig. 6J, the $CD4^+$ T cells number was at relatively low levels for the lung of the sham group and the ALI group, increased for BF and BF + NIR. However, the $CD8^+$ T cells number was similar in the sham group, ALI group and BF, slightly decreased for BF + NIR. After calculation, the MFI of $CD4^+$ T cells was 0.2 ± 0.1, 0.2 ± 0.1, 0.3 ± 0.1 and 0.3 ± 0.1, while it was 0.2 ± 0.1, 0.2 ± 0.1, 0.2 ± 0.1 and 0.1 ± 0.1 for $CD8^+$ T cell number in sham group, ALI group, BF and BF + NIR respectively (Supporting Information Fig. S23). And the corresponding $CD4^+/CD8^+$ ratio was 1.0 ± 0.1 (sham group), 0.8 ± 0.1 (ALI group), 1.5 ± 0.1 (BF) and 2.3 ± 0.2 (BF + NIR) (Fig. 6K). Thus, BF + NIR could increase the $CD4^+$ T cells number and the $CD4^+/CD8^+$ ratio in both of blood and lung tissue of rats, beneficial for ALI immunotherapy. However, for spleen tissue, the number of $CD4^+$ and

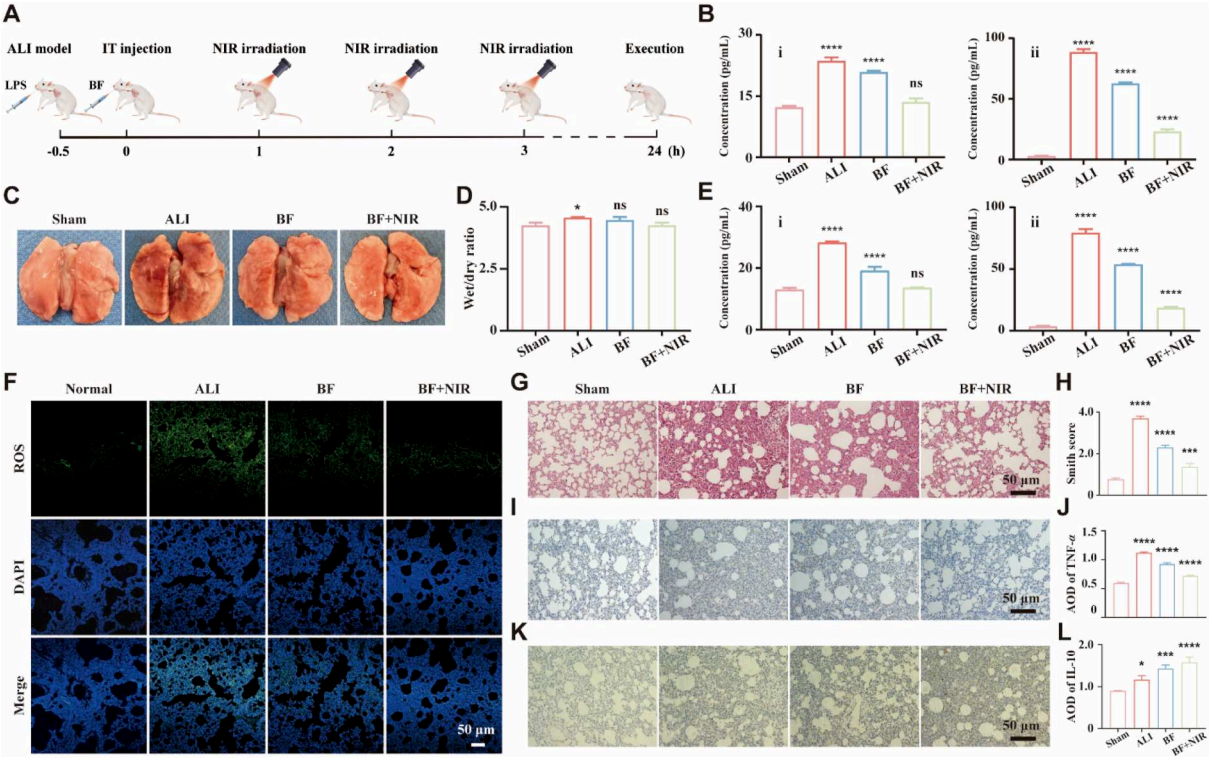

Figure 5 *In vivo* ALI therapy evaluation. (A) Time schedule of *in vivo* therapy. (B) The inflammatory factors (IL-6 (i) and TNF-α (ii)) expression levels in the blood serum of treated rats were measured by ELISA. (C) The macroscopic observation of the lung tissue of treated rats. (D) The wet/dry ratio of lung tissue of treated rats. (E) The inflammatory factors (IL-6 (i) and TNF-α (ii)) expression levels of lung homogenate of treated rats were measured by ELISA. (F) ROS levels of lung tissue of treated rats. (G) H&E staining images of lung tissue of treated rats, and the corresponding Smith score (H). (I) TNF-α expression levels of the lung tissue of treated rats, and the corresponding AOD (J). (K) IL-10 expression levels of the lung tissue of treated rats, and the corresponding AOD (L). Scale bar = 50 μm. Data are presented as mean ± SD (n = 6). The corresponding groups were: rats without treatment (sham group), and LPS-induced rats with saline injection (ALI group), BF injection (BF), and BF injection and NIR irradiation (BF + NIR). Data are expressed as mean ± SD. One-way ANOVA analysis was conducted to test for differences among groups. "*" symbol compared with sham group, *P < 0.05, **P < 0.01, ***P < 0.001, and ****P < 0.0001; and ns, not significant.

$CD8^+$ T cells was also analyzed by flow cytometry. As shown in Supporting Information Figs. S24 and S25, no prominent changes in $CD4^+$ and $CD8^+$ T cells number were observed, with a similar $CD4^+/CD8^+$ ratio for all groups. Generally, for acute disease' therapy, the changes of $CD4^+$ and $CD8^+$ T cells number in the spleen were not obviously observed[88].

Altogether, it had confirmed that the strategy of BF + NIR could efficiently achieve ALI immunotherapy *via* lowering CD86 expression and increasing CD206 expression to induce macrophage M2 directional polarization, and increasing the number of $CD4^+$ T cells and the $CD4^+/CD8^+$ ratio to activate immunoregulation.

3.8. *Anti-inflammation mechanism investigation*

The strategy of BF + NIR could efficiently scavenge ROS, lower inflammatory factors expression, induce macrophages M2 polarization, and activate immunoregulation. In the mechanism, WB was applied to detect the related proteins' expression levels. As shown in Supporting Information Figs. S26 and S27, Fig. 7A and B, the p65 expression was at relatively low levels for the normal group, while its expression was almost the same for the other groups. However, p-p65 and p-IκBα expression were at low levels for the normal group, significantly enhanced for the control group. And treatments could decrease their expression levels. Conversely, the IκBα expression was in relatively high levels for normal group compared to those of control group. After treatments, IκBα expression increased. After statistical analysis, the p-p65 and p-IκBα expression levels were 1.0 ± 0.1 and 0.8 ± 0.1 for the control group, decreased to 0.9 ± 0.1 and 0.7 ± 0.1 for BSA, 0.8 ± 0.1 and 0.6 ± 0.1 for BF, 0.4 ± 0.1 and 0.6 ± 0.1 for BF + NIR, and 0.3 ± 0.1 and 0.5 ± 0.1 for the normal group respectively (ii and iv of Fig. 7B). In contrast, the IκBα expression levels were 1.1 ± 0.1 in normal group, decreased to 0.6 ± 0.1 in control group. Compared to the control group, its expression levels increased to 0.7 ± 0.1, 0.7 ± 0.1 and 1.0 ± 0.1 in BSA, BF and BF + NIR respectively (iii of Fig. 7B).

Besides, their relative gene expression levels were analyzed by RT-qPCR. The detailed primer sequences are displayed in Supporting Information Table S7. As illustrated in i of Fig. 7C, at cellular levels, for p65 gene expression, it was at almost in similar levels for all groups. However, the p-p65 and p-IκBα gene expression levels were relatively low for the normal group (1.0 ± 0.1 and 1.0 ± 0.1), obviously increased to 4.5 ± 0.1 and 14.5 ± 0.3 for the control group. Compared to control group, they slightly decreased to 4.1 ± 0.1 and 12.5 ± 0.3 for BSA, and significantly decreased for BF (3.4 ± 0.3 and 11.1 ± 0.3) and BF + NIR (2.0 ± 0.1 and 5.4 ±0.9) (ii and iv of Fig. 7C). In

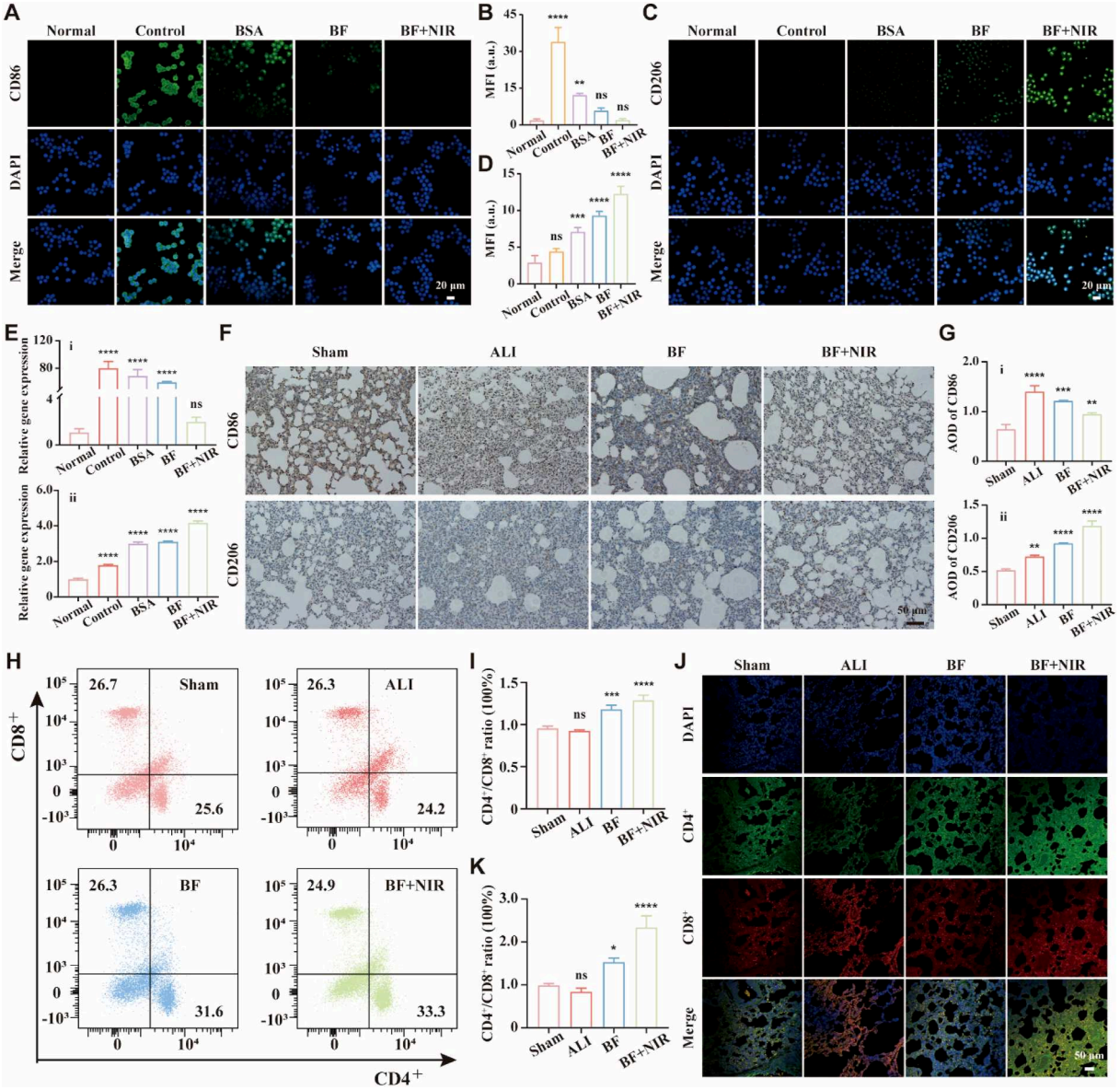

Figure 6 ALI immunotherapy evaluation. (A) CD86 expression levels of treated cells by fluorescent microscope, and the corresponding MFI (B). Scale bar = 20 μm. Data are presented as mean ± SD (n = 3). (C) CD206 expression levels of treated cells by fluorescent microscope, and the corresponding MFI (D). Scale bar = 20 μm. Data are presented as mean ± SD (n = 3). (E) Relative gene expression levels of treated cells by RT-qPCR: CD86 (i) and CD206 (ii). The corresponding groups were: cells without treatment (normal group), cells pre-treated with LPS followed by incubating with PBS (control group), 100 μg/mL BSA (BSA), 100 μg/mL BF (BF), and 100 μg/mL BF and NIR irradiation (2 W/cm^2) (BF + NIR). (F) CD86 and CD206 co-immunostaining images of lung tissue of treated rats, and the corresponding AOD (G): CD86 (i) and CD206 (ii). (H) Gating of the number of $CD4^+$ and $CD8^+$ T cells in the lung of treated rats by flow cytometry, and the corresponding $CD4^+/CD8^+$ ratio (I). (J) $CD4^+$ and $CD8^+$ T cells co-immunofluorescent staining images in the lung tissue of treated rats by fluorescent microscopy, and the corresponding $CD4^+/CD8^+$ ratio (K). Scale bar = 50 μm. Data are presented as mean ± SD (n = 6). The corresponding groups were: rats without treatment (sham group), and LPS-induced rats with saline injection (ALI group), BF injection (BF), and BF injection and NIR irradiation (BF + NIR). Data are expressed as mean ± SD. One-way ANOVA analysis was conducted to test for differences among groups. "*" symbol compared with normal or sham group, *P < 0.05, **P < 0.01, ***P < 0.001, and ****P < 0.0001; and ns, not significant.

particular, the IκBα gene expression was in relative high levels (0.9 ± 0.1) in normal group, significantly decreased to 0.1 ± 0.1 in the control group. After treatments, its expression had been improved, which was 0.6 ± 0.1, 0.7 ± 0.1 and 1.0 ± 0.1 in BSA, BF and BF + NIR, respectively (iii of Fig. 7C). Finally, in animal level, the expression levels of pathway-related proteins were also analyzed by immunofluorescent staining. As shown in Fig. 7D and E, the expression of p65 was in similar levels for all groups. Significantly, the p-p65 expression was in the lowest levels for the normal group (0.5 ± 0.1), and increased for ALI group (0.9 ± 0.1). Treatments could decrease its expression. Among them, BF + NIR (0.6 ± 0.1) played the most effective role. Thus,

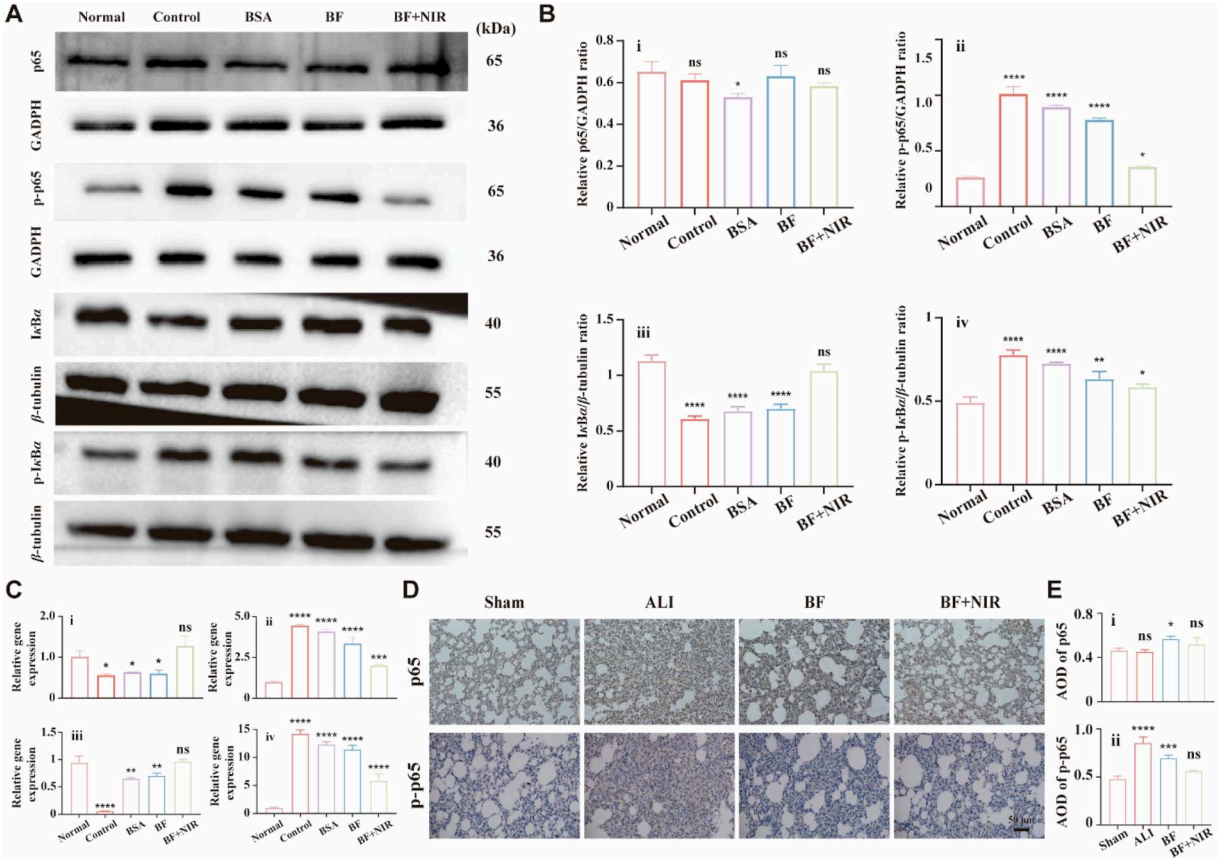

Figure 7 Relative therapeutic mechanism exploration. (A) Pathway-related proteins expression levels of treated cells, and the corresponding quantified results (B): p65 (i), p-p65 (ii), IκBα (iii) and p-IκBα (iv). (C) Pathway-related gene expression levels of treated cells by RT-qPCR. The corresponding groups were: cells without treatment (normal group), cells pre-treated with LPS followed by incubating with PBS (control group), 100 μg/mL BSA (BSA), 100 μg/mL BF (BF), and 100 μg/mL BF and NIR irradiation (2 W/cm^2) (BF + NIR). (D) p65 and p-p65 expression levels of the lung tissue of treated rats, and the corresponding AOD (K): p65 (i) and p-p65 (ii). Scale bar = 50 μm. Data are presented as mean ± SD (n = 6). The corresponding groups were: rats without treatment (sham group), and LPS-induced rats with saline injection (ALI group), BF injection (BF), and BF injection and NIR irradiation (BF + NIR). Data are expressed as mean ± SD. One-way ANOVA analysis was conducted to test for differences among groups. "*" symbol compared with normal or sham group, *P < 0.05, **P < 0.01, ***P < 0.001, and ****P < 0.0001; and ns, not significant.

BF + NIR could efficiently alleviate ALI *via* inhibiting the NF-κB pathway, revealed by the downregulation of p-p65 and p-IκBα expression.

4. Conclusions

In summary, an ultrasmall Fe_3O_4-loaded BSA nanocluster (BF) was developed to act as a nanozyme with enhanced ROS scavenging capacities for ALI immunotherapy. Combining with NIR irradiation, it was confirmed that BF possessed multiple enzymatic activities to scavenge ROS. In cellular level, compared to BSA and BF, the strategy of BF + NIR possessed excellent antioxidant and anti-inflammatory functions *via* lowering intracellular ROS levels, downregulating inflammatory factors expression levels, and upregulating tissue repair factors expression levels, to reprogram redox homeostasis and accelerate tissue repair for ALI therapy. Meanwhile, BF possessed good retention time and was gradually cleared in the lung by IT administration, no damage to other organs. In addition, BF + NIR strengthened the induction of macrophage M2 polarization, and an increase of $CD4^+/CD8^+$ T cell ratios, thereby leading to immunoregulation activation. Significantly, NF-κB pathway inhibition mediated an anti-inflammation mechanism has been proved both *in vitro* and *in vivo*. It finally provides a promising strategy of BF + NIR to achieve the synergistic enhancement of ALI immunotherapy with high efficacy and biosafety, which extends its applications for other inflammation related diseases.

Acknowledgments

This study was financially supported by the Joint Project on Regional High-Incidence Diseases Research of Guangxi Natural Science Foundation (Nos. 2024GXNSFAA010089 and 2025GXNSFBA069275, China), the National Natural Science Foundation of China (No. 82160902, China), the China Postdoctoral Science Foundation (No. 2024MD753921, China), the Key Laboratory of Micro-Nanoscale Bioanalysis and Drug Screening, Education Department of Guangxi Zhuang Autonomous Region (GXYWSX202404, China), the First-class Discipline Innovation-driven Talent Program of Guangxi Medical University, and the Major Talent Project of Guangxi Autonomous Region.

Author contributions

Xiaoxuan Guan, Binbin Zou, and Weiqian Jin conceived and planned the study. Yongfeng Lan, Jing Qian, and Juan Luo conducted the experimental work. Yanjun Lei, Xuzhi Liang, and Shiyu Zhang were responsible for analyzing the data. Yan Long, Chen Qian, and Chaoyu Huang contributed to specific experimental procedures. Yan Liu and Weili Tian assisted with technical and logistical support. Jiahao Huang, Ming Gao, and Lin Liao oversaw and coordinated the research. Yongrong Lai, Ming Gao, and Lin Liao edited and refined the manuscript. All of the authors have read and approved the final manuscript.

Conflicts of interest

The authors have no conflicts of interest to declare.

Appendix A. Supporting information

Supporting information to this article can be found online at https://doi.org/10.1016/j.apsb.2025.08.012.

References

1. Wick KD, Ware LB, Matthay MA. Acute respiratory distress syndrome. *BMJ* 2024;**387**:e076612.
2. Ji HY, Zhang CM, Xu FY, Mao QY, Xia R, Chen MQ, et al. Inhaled pro-efferocytic nanozymes promote resolution of acute lung injury. *Adv Sci* 2022;**26**:e2201696.
3. Ren ZX, Zheng ZH, Feng XJ. Role of gut microbes in acute lung injury/acute respiratory distress syndrome. *Gut Microbes* 2024;**16**: 2440125.
4. Wang Y, Hu LF, Liu NH, Yang JS, Xing L, Jeong JH, et al. Mitophagy-enhanced nanoparticle-engineered mitochondria restore homeostasis of mitochondrial pool for alleviating pulmonary fibrosis. *ACS Nano* 2024;**18**:32705−22.
5. Ding FX, Zhou M, Ren YY, Li Y, Xiang JY, Li YH, et al. Mitochondrial extracellular vesicles: a promising avenue for diagnosing and treating lung diseases. *ACS Nano* 2024;**18**:25372−404.
6. Han ZH, Gao X, Wang YJ, Cheng SN, Zhong XY, Xu Y, et al. Ultrasmall iron-quercetin metal natural product nanocomplex with antioxidant and macrophage regulation in rheumatoid arthritis. *Acta Pharm Sin B* 2023;**13**:1726−39.
7. Sun SC. The non-canonical NF-κB pathway in immunity and inflammation. *Nat Rev Immunol* 2017;**17**:545−58.
8. Zhang RF, Jiang B, Fan KL, Gao LZ, Yan XY. Designing nanozymes for *in vivo* applications. *Nat Rev Bioeng* 2024;**2**:849−68.
9. Yang JX, Xiao SH, Deng JJ, Li YQ, Hu H, Wang JW, et al. Oxygen vacancy-engineered cerium oxide mediated by copper-platinum exhibit enhanced SOD/CAT-mimicking activities to regulate the microenvironment for osteoarthritis therapy. *J Nanobiotechnol* 2024; **22**:491.
10. Taniguchi K, Karin M. NF-κB, inflammation, immunity and cancer: coming of age. *Nat Rev Immunol* 2018;**18**:309−24.
11. Gorman EA, O'Kane CM, McAuley DF. Acute respiratory distress syndrome in adults: diagnosis, outcomes, long-term sequelae, and management. *Lancet* 2022;**400**:1157−70.
12. Pang L, Liu CY, Gong GH, Quan ZS. Synthesis, *in vitro* and *in vivo* biological evaluation of novel lappaconitine derivatives as potential anti-inflammatory agents. *Acta Pharm Sin B* 2020;**10**:628−45.
13. Chen J, Zhu YF, Wu CT, Shi JL. Engineering lactate-modulating nanomedicines for cancer therapy. *Chem Soc Rev* 2023;**52**:973−1000.
14. Guo Q, Jin YZ, Chen XY, Ye XM, Shen X, Lin MX, et al. NF-κB in biology and targeted therapy: new insights and translational implications. *Signal Transduct Target Ther* 2024;**9**:53.
15. Li CF, Wei SQ, Sun DL, Yang Z, Wang Q, Lin H, et al. Development of RELB-targeting small-molecule inhibitors of non-canonical NF-κB signaling with antitumor efficacy. *Mol Ther* 2025;**33**:1519−34.
16. Yuan Y, Tian CY, Wang Q, Qiu XY, Wang YF, Jiang HL, et al. Synergistic amplification of ferroptosis with liposomal oxidation catalyst and GPX4 inhibitor for enhanced cancer therapy. *Adv Healthc Mater* 2023;**12**:e2301292.
17. Yan X, Liu X, Zhao CH, Chen GQ. Applications of synthetic biology in medical and pharmaceutical fields. *Signal Transduct Target Ther* 2023;**8**:199.
18. Zhou Y, Li QQ, Wu Y, Li XY, Zhou Y, Wang Z, et al. Molecularly stimuli-responsive self-assembled peptide nanoparticles for targeted imaging and therapy. *ACS Nano* 2023;**17**:8004−25.
19. Liu QQ, Gao ZX, Zhang XY, Duan QN, Zhang Y, Midgley AC, et al. Assembly of genetically engineered ionizable protein nanocage-based nanozymes for intracellular superoxide scavenging. *Nat Commun* 2025;**16**:1123.
20. Liu J, Dong SM, Gai SL, Dong YS, Liu B, Zhao ZY, et al. Design and mechanism insight of monodispersed AuCuPt alloy nanozyme with antitumor activity. *ACS Nano* 2023;**17**:20402−23.
21. Lu MZ, Wu HA, Liu D, Wang F, Wang Y, Wang MJ, et al. Camouflaged nanoreactors mediated radiotherapy-adjuvant chemodynamic synergistic therapy. *ACS Nano* 2023;**17**:24170−86.
22. Duan RX, Li YP, Zhang RR, Hu XL, Wang Y, Zeng JF, et al. Reversing acute kidney injury through coordinated interplay of anti-inflammation and iron supplementation. *Adv Mater* 2023;**35**: e2301283.
23. Chen ZX, Qi FG, Qiu WJ, Wu CY, Zong M, Ge M, et al. Hydrogenated germanene nanosheets as an antioxidative defense agent for acute kidney injury treatment. *Adv Sci* 2022;**9**:e2202933.
24. Qi L, Duan BW, Wang H, Liu YJ, Han H, Han MM, et al. Reactive oxygen species-responsive nanoparticles toward extracellular matrix normalization for pancreatic fibrosis regression. *Adv Sci* 2024;**11**: e2401254.
25. Xia XY, Li H, Xu XB, Zhao GH, Du M. Facilitating pro-survival mitophagy for alleviating Parkinson's disease *via* sequence-targeted lycopene nanodots. *ACS Nano* 2023;**17**:17979−95.
26. Zhao MJ, Kang MM, Wang JR, Yang RH, Zhong XP, Xie QH, et al. Stem cell-derived nanovesicles embedded in dual-layered hydrogel for programmed ROS regulation and comprehensive tissue regeneration in burn wound healing. *Adv Mater* 2024;**36**:e2401369.
27. Zhao YS, Zhao SQ, Du Y, Gao ZF, Li YL, Ma HM, et al. Inverse oxide/alloy-structured nanozymes with NIR-triggered enzymatic cascade regulation of ROS homeostasis for efficient wound healing. *Adv Mater* 2025;**37**:e2418731.
28. Chen T, Cai YP, Ren BY, Sánchez BJ, Dong RF. Intelligent micro/-nanorobots based on biotemplates. *Mater Horiz* 2024;**11**:2772−801.
29. Fromain A, Perez JE, Van de Walle A, Lalatonne Y, Wilhelm C. Photothermia at the nanoscale induces ferroptosis *via* nanoparticle degradation. *Nat Commun* 2023;**14**:4637.
30. Gao Y, Yang CD, Sun FL, He DP, Wang XQ, Chen J, et al. Ligand-tuning metallic sites in molecular complexes for efficient water oxidation. *Angew Chem Int Ed* 2025;**64**:e202415755.
31. Hu ZW, Tan HX, Ye YC, Xu WX, Gao JB, Liu L, et al. NIR-actuated ferroptosis nanomotor for enhanced tumor penetration and therapy. *Adv Mater* 2024;**36**:e2412227.
32. Xia YQ, Chen ZX, Zhang XH, Yang P, Wang ZL. Phosphatidylcholine liposome accelerated platinum nanomachines (PLANEs) with enhanced penetration capability for thrombus mechanotherapy. *Adv Mater* 2025;**24**:e2418590.
33. Qi XL, Ge XX, Chen XJ, Cai EY, Xiang YJ, Xu HB, et al. An immunoregulation hydrogel with controlled hyperthermia-augmented oxygenation and ROS scavenging for treating diabetic foot ulcers. *Adv Funct Mater* 2024;**34**:e2400489.
34. Liu XD, Zhang HF, Yan BC, Yeung KWK, Liao Y, Ouyang LP, et al. On-off phagocytosis and switchable macrophage activation stimulated with NIR for infected percutaneous tissue repair of polypyrrole-coated sulfonated PEEK. *Adv Sci* 2023;**10**:e220−5048.

35. Li Y, Liu DF, Chen T, Song JW, Yu XY, Liu Q, et al. Inhaled NIR-II nanocatalysts for real-time monitoring and immunomodulatory therapy of acute lung injury. *Adv Funct Mater* 2024;**34**:e202403183.
36. Duan HX, Liu YH, Gao ZG, Huang W. Recent advances in drug delivery systems for targeting cancer stem cells. *Acta Pharm Sin B* 2021;**11**:55−70.
37. Qi JH, Wang Y, Chen H, Wu KT, Zhou P, Dou Y, et al. Advancing the Identification of bioactive molecules and the construction of a synergistic drug delivery system in combating lung injury. *Adv Sci* 2025;**12**:e2407802.
38. Liu C, Xi L, Liu YH, Mak JCW, Mao SR, Wang ZP, et al. An inhalable hybrid biomimetic nanoplatform for sequential drug release and remodeling lung immune homeostasis in acute lung injury treatment. *ACS Nano* 2023;**17**:11626−44.
39. Murphy G, Brayden DJ, Cheung DL, Liew A, Fitzgerald M, Pandit A. Albumin-based delivery systems: recent advances, challenges, and opportunities. *J Control Release* 2025;**380**:375−95.
40. Lantzberg B, Zeyn Y, Forster R, Jian L, Schauenburg D, Hieber C, et al. Glycogen-inspired trimannosylated serum albumin nanocarriers for targeted delivery of toll-like receptor 7/8 agonists to immune cells and liver. *J Control Release* 2025;**382**:113705.
41. Wu SQ, Tang Q, Fang WF, Sun Z, Zhang M, Liu E, et al. Targeting stem-property and vasculogenic mimicry for sensitizing paclitaxel therapy of triple-negative breast cancer by biomimetic codelivery. *Acta Pharm Sin B* 2025;**15**:3226−42.
42. Wang YN, Liu XH, Li KY, Wang XY, Zhang X, Qian DY, et al. Self-sulfhydrated, nitro-fixed albumin nanoparticles as a potent therapeutic agent for the treatment of acute liver injury. *ACS Nano* 2024;**18**:20772−91.
43. Ding H, Cui Y, Yang J, Li Y, Zhang HT, Ju S, et al. ROS-responsive microneedles loaded with integrin avβ6-blocking antibodies for the treatment of pulmonary fibrosis. *J Control Release* 2023;**360**:365−75.
44. Lei DD, Liao L, Qin T, Guan XX, Duan KP, Gao ZW, et al. Reprogramming lung redox homeostasis by NIR driven ultra-small Pd loaded covalent organic framework inhibits NF-κB pathway for acute lung injury immunotherapy. *Adv Sci* 2025;**12**:e2413697.
45. Wu XS, Wang BL, Li YC, Guan XX, Yin MJ, Lv WQ, et al. NIR driven catalytic enhanced acute lung injury therapy by using polydopamine@Co nanozyme *via* scavenging ROS. *Chin Chem Lett* 2025;**36**:110211.
46. Xu D, Yang F, Chen JY, Zhu TX, Wang F, Xiao YT, et al. Novel STING-targeted PET radiotracer for alert and therapeutic evaluation of acute lung injury. *Acta Pharm Sin B* 2023;**13**:2124−37.
47. Zou Q, Chen X, Li BJ, Zhang RJ, Pan JB, Zhang XJ, et al. Bioinspired BSA@polydopamine@Fe nanoprobe with self-purification capacity for targeted magnetic resonance imaging of acute kidney injury. *ACS Nano* 2024;**18**:4783−95.
48. Li BC, Yang J, Lu SR, Zhao JQ, Du YH, Cai YP, et al. Chlorella-based biohybrid microrobot for removing both nutrient and microalgae toward efficient water eutrophication treatment. *Nano Lett* 2025;**25**:48−55.
49. Abbigeri MB, Thokchom B, Singh SR, Bhavi SM, Harini BP, Yarajarla RB. Antioxidant and anti-diabetic potential of the green synthesized silver nanoparticles using *Martynia annua* L. root extract. *Nano Trans Med* 2025;**4**:100070.
50. Li Z, Xie CJ, Ren XW, Zhang Q, Ma BJ. CuS nanoenzyme against bacterial infection by *in situ* hydroxyl radical generation on bacteria surface. *Rare Met* 2023;**42**:1899−911.
51. Wang HF, Chen S, He ZH, Chen JY, Zhu Z, Wan QB, et al. Synthesis and potential osteogenic applications of Wnt3a-loaded ZIF-8 nanoparticles. *Chin Chem Lett* 2024;**35**:108597.
52. Lim SH, Wong TW, Tay WX. Overcoming colloidal nanoparticle aggregation in biological milieu for cancer therapeutic delivery: perspectives of materials and particle design. *Adv Colloid Interface Sci* 2024;**325**:103094.
53. Chen J, Wang B, Shen L, Huang YZ. Microalgae-carrying nanomedicine for bioadhesive drug delivery for treating chemotherapy-induced intestinal injury. *Asian J Pharm Sci* 2025;**20**:101024.
54. Jin WQ, Liao L, Qin T, Guan XX, Gao HY, Liang P, et al. Recent advances in nanomedicine therapy for bacterial pneumonia. *Chin Chem Lett* 2025;**36**:110920.
55. Gao X, Han ZH, Huang C, Lei HL, Li GQ, Chen L, et al. An anti-inflammatory and neuroprotective biomimetic nanoplatform for repairing spinal cord injury. *Bioact Mater* 2022;**18**:569−82.
56. Xu YN, Yang L, Li M, Shu HZ, Jia N, Gao YZ, et al. Anti-osteosarcoma trimodal synergistic therapy using NiFe-LDH and MXene nanocomposite for enhanced biocompatibility and efficacy. *Acta Pharm Sin B* 2024;**14**:1329−44.
57. Cao WR, Zhang X, Chen JX, Sun L, He HN, Yu F. Codelivery of apigenin, FdUMP and CD276 antibody synergistic inhibit colorectal cancer by ferroptosis-apoptosis-pyroptosis and CD276 blockade. *Asian J Pharm Sci* 2025;**20**:101016.
58. Wang H, Ouyang WR, Liu HX. Tumor microenvironment responsive nanozymes for multimodal imaging of tumors. *Nano Trans Med* 2024;**3**:100032.
59. Tu Z, Wan Y, Ge J, Li CC, Liang T, Li Z. NIR-IIb-triggered photodynamic therapy combined with chemotherapy platform based on rare-earth-doped nanoparticles. *Rare Met* 2024;**43**:3220−31.
60. Huang J, Deng GM, Wang SY, Zhao TJ, Chen QH, Yang YQ, et al. A NIR-II photoactivatable "ROS bomb" with high-density Cu_2O-supported MoS_2 nanoflowers for anticancer therapy. *Adv Sci* 2023;**10**:e2302208.
61. Richards CJ, Burgers TCQ, Vlijm R, Roos WH, Åberg C. Rapid internalization of nanoparticles by human cells at the single particle level. *ACS Nano* 2023;**17**:16517−29.
62. Wang Z, Pan BS, Manne RK, Chen JG, Lv DW, Wang MM, et al. CD36-mediated endocytosis of proteolysis-targeting chimeras. *Cell* 2025;**188**:3219−37.
63. Sardar P, Beresford-Jones BS, Xia WMY, Shabana O, Suyama S, Ramos RJF, et al. Gut microbiota-derived hexa-acylated lipopolysaccharides enhance cancer immunotherapy responses. *Nat Microbiol* 2025;**10**:795−807.
64. Hering M, Madi A, Sandhoff R, Ma S, Wu JX, Mieg A, et al. Sphinganine recruits TLR4 adaptors in macrophages and promotes inflammation in murine models of sepsis and melanoma. *Nat Commun* 2024;**15**:6067.
65. Zhang J, Zhang M, Zhu QM, Xu XR, Feng YL, Lin S, et al. Allosteric regulation of Keap1 by 8β-hydroxy-α-cyclocostunolide for the treatment of acute lung injury. *Acta Pharm Sin B* 2024;**14**:4174−8.
66. Su F, Zhang C, Zhang QY, Shen Y, Li SQ, Shi JL, et al. Multifaceted immunomodulatory nanocomplexes target neutrophilic-ROS inflammation in acute lung injury. *Adv Sci* 2025;**12**:e2411823.
67. Ji HX, Zheng ZY, Li SQ, Xiao X, Tang WX, Zhang XH, et al. Research progress of serum albumin in the field of drug delivery. *IMed* 2024;**2**:e20240010.
68. Dong SH, Cao HL, Yuan Y, Liang S, Fu ZD, Shi W, et al. A novel "three-in-one" copper-based metal-organic framework nanozyme eradicates colorectal cancer and overcomes chemoresistance for tumor therapy. *Adv Sci* 2025;**12**:e2413422.
69. Zhang CG, Cai YT, Pengrui D, Wang JC, Wang L, Xu JY, et al. Hollow mesoporous organosilica nanoparticles reduced graphene oxide based nanosystem for multimodal image-guided photothermal/photodynamic/chemo combinational therapy triggered by near-infrared. *Cell Prolif* 2023;**56**:e13443.
70. Xu MM, Lin CL, Zhao S, Zhang WD, Li D, Fang FH, et al. A versatile catalytic and photothermal lateral flow immunoassay based on ultrathin Fe-MoS_2 nanosheets for sensitive and accurate detection of influenza A. *View* 2024;**5**:20240067.
71. Wu P, Liu XN, Duan YH, Pan LP, Sun ZG, Chu HQ, et al. ZnPc photosensitizer-loaded peony-shaped $FeSe_2$ remotely controlled by near-infrared light for antimycobacterial therapy. *Acta Mater Med* 2023;**2**:260−9.
72. Yadav D, Malviya R. Novel nanomaterials as photo-activated cancer diagnostics and therapy. *Med Adv* 2023;**1**:190−209.
73. Yu YL, Li SJ, Yao Y, Shen XR, Li L, Huang Y. Increasing stiffness promotes pulmonary retention of ligand-directed dexamethasone-

loaded nanoparticle for enhanced acute lung inflammation therapy. *Bioact Mater* 2023;**20**:539−47.
74. Wang J, Gao X, Feng L, Zhang DL, Lv SH, Li XY, et al. Advances in near-infrared responsive functional nanocomposites for bioimaging and antitumor research. *J Control Release* 2025;**384**:113904.
75. Xue DZ, Wang YH, Zhang HJ. Advances of NIR light responsive materials for diagnosis and treatment of brain diseases. *Adv Opt Mater* 2023;**11**:2202888.
76. Zhang WJ, Jin LG, Wu SL, Wang CF, Zheng YF, Li ZY, et al. Microwave excited hyperthermy and catalysis of heterostructured Au/Cu−BTA for effective bacteria killing by accelerating charge separation. *Rare Met* 2024;**43**:5186−201.
77. Li XX, Wang W, Gao QX, Lai SS, Liu Y, Zhou ST, et al. Intelligent bacteria-targeting ZIF-8 composite for fluorescence imaging-guided photodynamic therapy of drug-resistant superbug infections and burn wound healing. *Exploration* 2024;**4**:20230113.
78. Tang DD, Xu NG, Fu YY, Peng W, Wu JS, Liu H, et al. Rationally designed an innovative proximity labeling near-infrared fluorogenic probe for imaging of peroxynitrite in acute lung injury. *Chin Chem Lett* 2025;**36**:110082.
79. Huang WC, Wen LH, Tian H, Jiang JM, Liu MH, Ye YC, et al. Self-propelled proteomotors with active cell-free mtDNA clearance for enhanced therapy of sepsis-associated acute lung injury. *Adv Sci* 2023;**10**:e2301635.
80. Ma JY, Ao YC, Yue Z, Wang ZQ, Hou XY, Li HB, et al. Elevated GFI1 in alveolar macrophages suppresses aCOD1 expression and exacerbates lipopolysaccharide-Induced lung injury in obesity. *Adv Sci* 2025;**12**:e2413546.
81. Friis KP, Gracin S, Oag S, Leijon A, Sand E, Lindberg B, et al. Spray dried lipid nanoparticle formulations enable intratracheal delivery of mRNA. *J Control Release* 2023;**363**:389−401.
82. Yan JY, Tang ZM, Li YN, Wang H, Hsu JC, Shi MM, et al. Molybdenum nanodots for acute lung injury therapy. *ACS Nano* 2023;**17**:23872−88.
83. Yi XZ, Gao JY, Wang Z. The human lung microbiome—a hidden link between microbes and human health and diseases. *iMeta* 2022;**1**:e33.
84. Chen NY, Zhou QQ, Jia ZF, Cheng N, Zhang S, Chen WD, et al. Enhancing cancer immunotherapy: nanotechnology-mediated immunotherapy overcoming immunosuppression. *Acta Pharm Sin B* 2024;**14**:3834−54.
85. Huang YT, Liu XL, Zhu JW, Chen ZJ, Yu L, Huang X, et al. Enzyme core spherical nucleic acid that enables enhanced cuproptosis and antitumor immune response through alleviating tumor hypoxia. *J Am Chem Soc* 2024;**146**:13805−16.
86. Luo Y, He XJ, Du QY, Xu L, Xu J, Wang JR, et al. Metal-based smart nanosystems in cancer immunotherapy. *Exploration* 2024;**4**:20230134.
87. Dong H, Li Q, Zhang Y, Ding M, Teng ZG, Mou YB. Biomaterials facilitating dendritic cell-mediated cancer immunotherapy. *Adv Sci* 2023;**10**:2301339.
88. Chu T, Wu M, Hoellbacher B, de Almeida GP, Wurmser C, Berner J, et al. Precursors of exhausted T cells are pre-emptively formed in acute infection. *Nature* 2025;**640**:782−92.